THE UNIVERSITY OF TOKYO

MASTER'S THESIS
修士論文

Position Sensorless and Energy-efficient Electromagnetic Levitation for Translational Motion Conveyor System

– Smart use of high frequency switching noise –

リニア搬送システム用の位置センサレスでエネルギー効率の良い電磁吸引浮上制御
– 高周波スイッチング雑音の賢い利用–

Author:
Salman Ahmed
Student ID: 37-145015

Supervisor:
Prof. Takafumi Koseki

A thesis submitted in fulfillment of the requirements
for the degree of Master of Engineering

in the

Department of Electrical Engineering and Information Systems
Graduate School of Engineering
The University of Tokyo

Submitted: August 26, 2016

Declaration of Authorship

I, Salman Ahmed
Student ID: 37-145015, declare that this thesis titled, “Position Sensorless and Energy-efficient Electromagnetic Levitation for Translational Motion Conveyor System
– Smart use of high frequency switching noise – ” and the work presented in it are my own. I confirm that:

- This work was done wholly or mainly while in candidature for a research degree at this University.
- Where any part of this thesis has previously been submitted for a degree or any other qualification at this University or any other institution, this has been clearly stated.
- Where I have consulted the published work of others, this is always clearly attributed.
- Where I have quoted from the work of others, the source is always given. With the exception of such quotations, this thesis is entirely my own work.
- I have acknowledged all main sources of help.
- Where the thesis is based on work done by myself jointly with others, I have made clear exactly what was done by others and what I have contributed myself.

Signed:

Date:

Abstract

Electromagnetic levitation (EML) technology is an old concept and has been the target of research for over three decades. Most research has been for high speed transportation but EML's merits can also be applied for industrial use. Cutting edge research has been applied for the field of active magnetic bearings, conveyor systems, precision machinery, EM launchers etc. But unfortunately, this technology has not become a widely used phenomenon even after decades of academic contributions. It is attributed to the complex, unstable and high cost nature of EML technology. This dissertation is focused on development of a simple, robust and low cost EML system that can be employed for translational motion conveyor system in industry.

Major cost contributing factors for any EML system include: 1) Requirement of constant power to counter the force of gravity which constitutes operational cost. 2) Since EML is inherently an unstable system, it requires constant feedback control. Unlike stable systems, additional hardware is required to achieve stabilization constituting equipment cost. The controlled physical quantity, air gap, monitored by displacement sensors form the major portion of the control equipment cost. By removal of this sensor, drastic cost reduction is achievable. This forms the motivation for sensorless/self-sensing EML systems.

Sensorless EML replaces the actual air gap sensor by terminal voltage and current measurements as virtual sensor estimating the required air gap signal. There has been considerable work in this field, the most noticeable being use of high frequency switching noise. By using switching amplifiers, high frequency voltage is injected into the coils and resulting triangular current waveform is measured. With ease of availability of low cost and high processing digital computers, the current-ripple is sampled multiple times. These samples are used to calculate the rising and falling ripple slope from which inductance and hence air gap is estimated. The method of slope measurement is normally influenced by variation of duty ratio of switching amplifier which affects the interval of rising/falling current that can be sampled. More samples mean accurate estimation. However, such is not the case since as a result of constant control law execution, duty ratio changes and hence the corresponding rising and falling intervals of current-ripple. This causes varying noise in air gap signal. To compensate it, we have proposed a method which uses a weighted contribution from both slopes that translates to a constant and low noise variance in the air gap signal.

Noise variance in air gap signal is an important performance parameter to establish an acceptable dynamic control for EML system. By combining the proposed sensorless method with state observer and disturbance observer, a noise suppression strategy is also proposed to attenuate the noise which propagates from current measurement all the way to the air gap. Ease of use for industrial engineer is established by reducing the tuning parameters for each observer to a single parameter, the corresponding time constant.

Steady state energy consumption by the levitating carrier is reduced by employing permanent magnets. An energy efficient method, known as zero power control that maintains a zero average current is applied in conjunction with sensorless method to demonstrate a truly cost effective EML system. This smart combination pair is claimed and verified as complimentary since each enhanced other's performance. Zero average current results in duty ratio vicinity around 0.5 which is the optimal situation for sensorless method. Furthermore, since zero power control is in fact a reference current tracking control and not a position tracking one, the need for an exact air gap position is redundant. A sufficiently low noise variance air gap signal with possible off set error obtain from low cost sensorless method is a thought as a viable bargain.

Finally, the research is concluded by considering the higher degree of motion topologies for sensorless EML system and its coordination with linear actuators which shall be pursued in future.

Acknowledgements

Firstly, I wish to express my gratitude to Almighty Allah, for blessing me with a sound mind, peace of heart and good health which has enabled me to achieve this prestigious goal.

I would like to express my deepest gratitude to my respected supervisor, Prof. Takafumi Koseki, for his expert suggestions and guidance throughout the duration of my master course as well as his concern and advices related to daily life. It was due to him that I was able to visit Koseki laboratory prior to enrollment and that paved way for me to pursue masters here. Technical meetings with Prof. Koseki have helped me develop my intellectual skills and have altered my way of thinking about control theory and electric machines. He has supported me in my ideas with critical and productive guidance. In time of need, Prof. Koseki has always arranged technical meetings out of his busy schedule. Lastly, I am grateful to him for making me part of Koseki Laboratory as well as accepting me as a Doctoral candidate.

I wish to thank Prof. Mimpei Morishita for his wise counsel regarding the future of magnetic levitation technology. His keen industrial insight has helped me to think more critically about prospective applications of my research. I am grateful to Prof. Akira Chiba and Prof. Hiroya Sugimoto of Chiba Laboratory, Titech, for allowing me to visit their laboratory and having constructive discussions on active magnetic bearings.

Furthermore, I wish to convey my profound gratitude to Ministry of Education, Culture, Sports, Science and Technology of Japan (Monbukagakusho) for continuous financial support throughout this course ensuring my sole concentration on studies and allowing me this opportunity to experience Japanese culture. In this regard, I also wish to thank Ms.Yoshie Minegishi and Ms. Yukimi Umeda of the IME program, Graduate School of Engineering for their timely correspondence and guidance to gain entrance to this prestigious university.

My thanks and appreciations also go to the members of Koseki laboratory for providing an intellectual and friendly environment for research, with special mentions to Mr. Duc Van Doan for his excellent input to my research. Discussions with him were always effective. He has helped me not just in research but also daily activities. I also would like to thank Mr. Hiroki Narita for being my tutor as well as giving technical advice in assembling my experimental test bench. Finally, Mr. Shoichiro Watanabe, Mr. Takada and Ms. Matsuzaki for their essential and exceptional management of lab activities.

Lastly, thanks to my parents for their countless prayers and moral support, and to my caring, loving and supportive wife, Afrah, for being by my side and encouraging me while I was completing my research.

Contents

List of Figures

List of Tables

To my parents,

The reason of what I became today.

Thank you for your great support and continuous care.

To my beloved wife,
For supporting me all the way.

Chapter 1

Introduction

1.1 Background

Magnetic levitation (MagLev) is a contact-less support technology which uses magnetic force to counter the effects of gravity. Contact-less suspension comes with futuristic benefits of zero friction allowing greater speeds, vibration isolation [1], low noise and zero dust emissions. These factors have always been a driving force for continuous efforts in academic and commercial research on Magnetic levitation. MagLev is conventionally divided into two categories, 1) Electromagnetic suspension (EMS) which uses electromagnetic coils to generate attractive force and is inherently unstable system and 2) Electrodynamic Suspension (EDS) which uses superconducting coils to generate repulsive forces for levitation and is a stable system. A prominent commercial comparison between these two categories is the Shanghai Maglev (Fig. 1.1(a)) based on EMS German technology and SCMaglev (superconducting MagLev) based on EDS technology in Japan (Fig. 1.1(b)).

Electromagnetic Suspension/Levitation (EML) is the focus of our research. Maglev is always associated with high speed transportation and it is true to some extent since its commercial display is as high speed trains. But MagLev has also found its way in industrial applications such a magnetic bearings [4], precision machinery [5], factory conveyor systems [6, 7, 8] etc. Even though research is being conducted from two or three decades, there are only few commercial products in industry. One of the main reason is attributed to system cost, operational and initial. Efforts to reduce steady state electric power have been extensively research upon. An efficient method called zero power control was introduced by Morishita [9] which ensures zero steady state average coil current. Many have furthered this concept in the past two decades [10, 6, 1], but industry engineers still remain adamant to welcome EML technology owing to its cost and complex nature.

Electromagnetic Suspension/Levitation (EML) being an unstable system requires active feedback and therefore the controlled physical quantity, air gap, is of utmost significance for stabilization. But air gap sensors form major portion of the total cost of any EML system. Removing them allows for drastic cost reduction. Not only this, but

(a) (b)

Figure 1.1: (a) Shanghai Maglev based on German EMS Transrapid technology [2]. (b) Superconducting Maglev based on EDS technology in Japan [3].

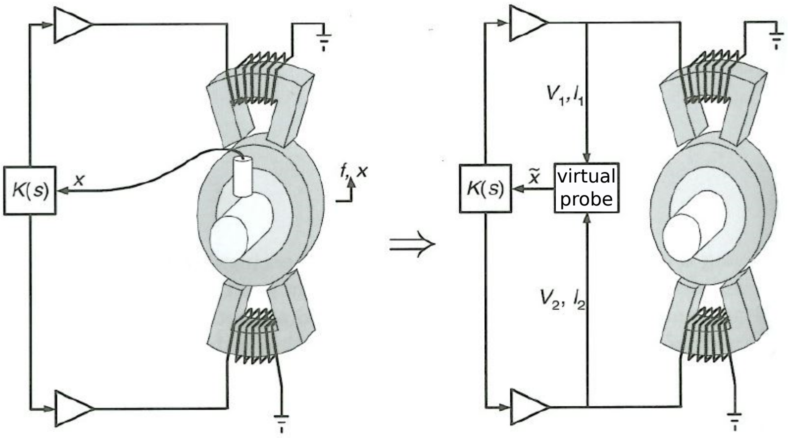

Figure 1.2: Sensorless/self-sensing EML topology [11]

stabilization without gap sensors adds redundancy, reliability, allows operation in harsh condition and simplifies wiring connections [11]. Therefore, a robust, simple and low cost sensorless EML system could aid in magnetic levitation technology being used in industrial applications.

1.1.1 Sensorless/Self-sensing Electromagnetic Levitation

Sensorless or self-sensing EML uses the current and voltage measurements as a virtual displacement sensor as shown in Fig. 1.2. The basics of sensorless EML is to estimate the system inductance by signal processing the current and voltage measurements and using accurate system model to detect air gap from the estimated inductance. The sensorless EML is divided into two types.

- Observer based estimation that considers the system as Linear Time Invariant (LTI) and uses the conventional Luenberger observer to estimate the air gap using current

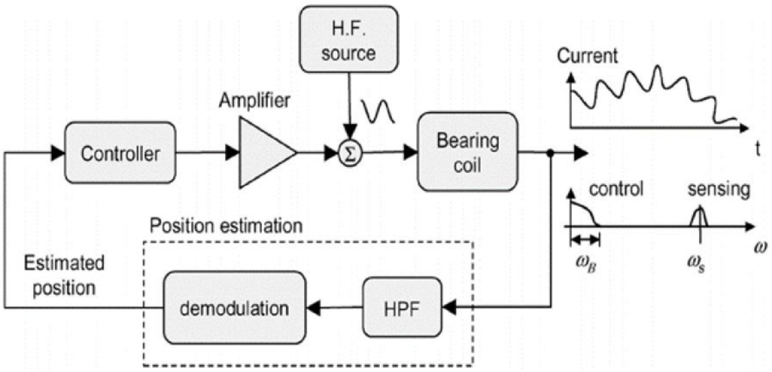

Figure 1.3: Concept of demodulation of current-ripple. [16]

state as an output signal. The system is shown to be observable under such assumption of LTI system [12]. However, it lacks robustness and is sensitive to system parameter variations as theoretically shown in [13].

- A deliberate voltage perturbation is injected into the system and the resulting coil current ripple is then measured and passed through signal processing filters to obtain an estimate of air gap as shown in Fig. 1.3. It was first demonstrated by Okada [14]. This was later modeled as Linear Time Periodic (LTP) process and was shown to have improved robustness in comparison to the Observer based method [15].

High frequency injection methods have been mostly researched upon owing to their enhanced robustness. Also since industrially wide spread and energy efficient switching amplifiers (Inverters/H-bridges) allow injection of high frequency without additional hardware. These methods are further categorized into two types.

One method is to use demodulation techniques to filter the current ripple and extract out the air gap. An observer like method [17] was presented which estimates the air gap using error between Band Pass Filtered (BPF) measured current and real time simulated BPF current. Relatively newer approach demonstrates the compensation of duty cycle variation and magnetic non-linearity by utilizing BPF voltage and current measurements[16]. A recent work demonstrated compensation of cross-coupling and saturation collectively by using a non-linear MIMO estimator and implementation on an 8 pole Active Magnetic Bearing (AMB)[18]. The demodulation approach has its demerits that it induces phase delays inherent in the high pass filter (HPF) and low pass filter (LPF). Furthermore, the duty cycle variation is compensated using additional voltage sensor.

The second category uses a simple approach of estimating the current-ripple slope directly. This was first time presented in [19]. However, the method used additional coil for detecting current change rate. Since then, as a consequence of the availability of low cost and high speed processing hardware, research has been conducted in directly measuring the coil current rate and estimating air gap as in [20, 21, 22, 23, 24, 25].

In [25] high speed ADCs are used to obtain multiple current samples and calculate the current slope. By using double slopes, the shift of resistance due to temperature change is mathematically compensated by using both voltage and current measurements. Similar results are presented in [23] by using only a current sensors. However, this is achieved at the expense of division of switching period of the power amplifier into a dedicated sensing period of a constant duty cycle. The same approach of division is also presented in [20]. The consequence of switching period division is the decrease in the available DC voltage to 50%. As a result, the current control dynamics deteriorate. It also introduces a dead time of 2 switching periods between estimation and control effort generation. This shows that there still exists possibilities for further improvement in the sensorless methods.

1.2 Motivation for Sensorless Air gap Detection

Firstly, most of the work in sensorless EML is focused on implementation on Active Magnetic Bearings (AMB). The application of sensorless EML for large air gap translational motion conveyors, to the best of author's knowledge, is not explicitly present in literature. Large air gap EML systems have different conditions than the AMB. One obvious difference is in the operating range of air gap which is $x(t) < 1$[mm] for AMB and $x(t) = 8{\sim}10$[mm] for translational motion conveyors. At large air gap, the sensitivity of inductance to the change in air gap is drastically reduced due to the leakage flux and fringing effects. This puts tighter constraints of noise on the air gap detection algorithm. Furthermore, AMB being relatively small scale than translational motion conveyors has the luxury of using high quality material for cores which have less eddy current losses. Whereas large eddy currents are induced in non-laminated iron rails, which leaves the portion of sampled current-ripple useless for slope estimation [26].

Secondly, in relation to the sensorless method itself, air gap detection relies strongly on current sensor measurement, significant amount of noise degrades accuracy of the detection algorithm. Furthermore, an effective estimate of current-ripple slope requires a threshold on the minimum number of current samples. This was done by fixing the duty cycle range in [25] or by having a dedicated sensing cycle in[23]. Limiting duty ratio range reduces the overall available DC voltage and consequently control performance. Furthermore, the varying duty ratio directly influences the noise in estimated air gap signal.

With the above reasons in mind and the fact that there is almost no commendable work in sensorless EML for translational conveyors, this research focuses on improving the short comings of the sensorless methods and take up the necessary steps to implement the proposed improved methods for large air gap translational motion conveyors. Furthermore, an additional step is taken to ensure minimum operational cost of EML systems by employing the well matured concept of zero power control [9]. This reduction of both system and operational cost provides possibilities for EML to become wide spread for industrial use.

1.3 Outline of Research

The research outline is shown in Fig. 1.4. In the second chapter a comprehensive analysis of a simple C-core electromagnet is conducted. The relevant equations are derived analytically. Followed by a numerical simulation carried out in JMAG CAD software. Finally in chapter 2 the experimental test bench is introduced on which all of the proposed methods of this research are experimentally verified. The Chapter is concluded with experimental identification of plant parameters.

In Chapter 3, conventional control techniques are introduced. Since EML is unstable, any kind of performance analysis cannot be performed. Therefore at first a stable EML system is obtained. A simple Proportional-Derivative (PD) controller is designed using Manabe's coefficient method [27]. The designed controller is numerically and experimentally verified. Following PD control, state feedback controller is designed which forms the basis of zero power control which is introduced later in Chapter 5.

The core part of this research lies in Chapter 4 which is the sensorless EML methods. A novel method named single slope detection is introduced first which ensures a minimum error threshold on slope calculation by using either rising part of current-ripple or falling part. This division is decided based on prior calculation of duty ratio for successive time periods. Single slope detection is found to be susceptible to resistance change. To counter that, a resistance estimation formula is derived. Proceeding forward, weighted current-ripple slope measurement method is introduced which has low noise variance of double slope method and has robustness of single slope detection towards variation of duty ratio. A comprehensive statistical analysis is also carried out to show the goodness of the proposed method. The chapter is concluded with a noise suppression strategy by using a combination of state observer and disturbance observer along with the proposed sensorless method. All proposed methods and strategies are experimentally verified on the test bench.

In chapter 5, a smart combination of sensorless EML with zero power control is introduced. The author's claim that zero power control and proposed sensorless method are a complimentary pair which enhance each other's performances is verified by experimental demonstration. The chapter ends at analyzing some improvements to the PM assisted EML systems. The results are promising and show good prospects for future industrial use. The research is concluded in chapter 6 and future works are discussed.

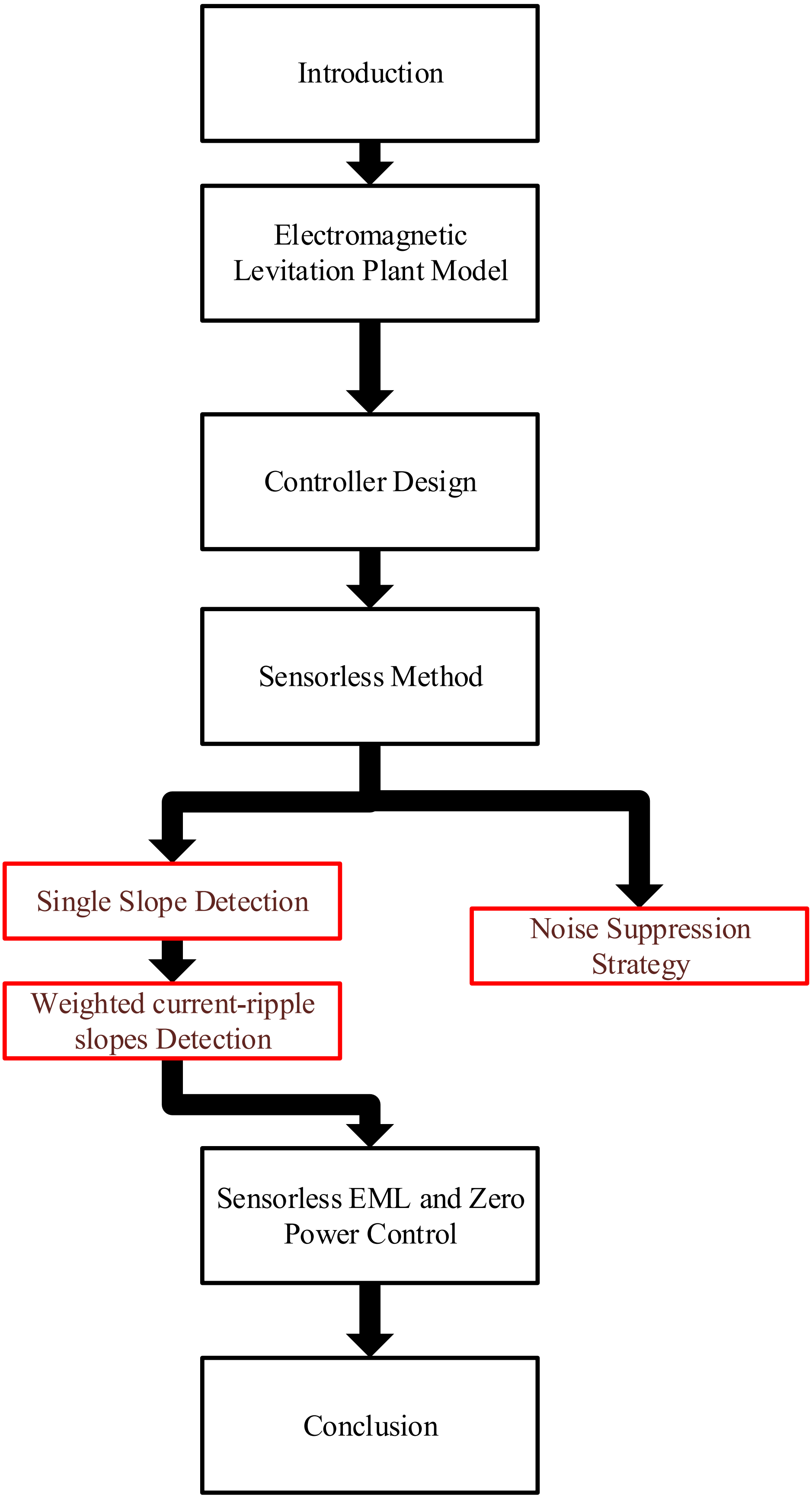

Figure 1.4: Research Outline.

Chapter 2

Analysis of EML Plant and Experimental Parameters Identification

2.1 Simplified Electromagnetic Modeling

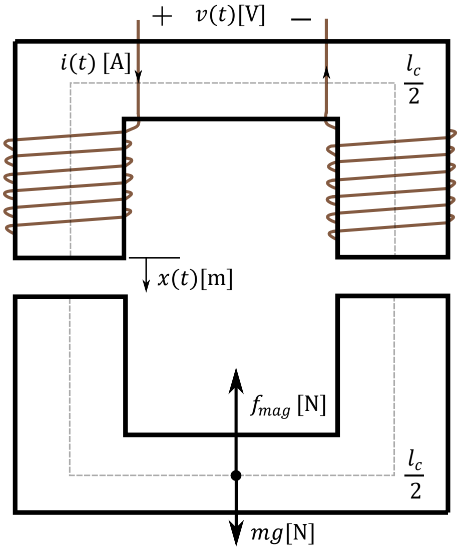

Figure 2.1: Electromagnetic Levitation (EML) plant

An accurate model of the Electromagnetic levitation system is essential for design of control and the air gap detection algorithm. Figure 2.1 shows a typical EML system in which the upper part is fixed and the lower one can move vertically. Table 2.1 shows the description of the parameters used in the mathematical model of EML. Using Newton's second law and Faraday's law, we define the dynamic relations of the EML system as:

$$m\ddot{x}(t) = -f_{mag} + mg \tag{2.1}$$

$$v(t) = i(t)R + \frac{d\lambda}{dt} \tag{2.2}$$

The above two equations represent the electrical and mechanical domains linked via the magnetic quantity, flux ϕ. This link is expressed using the following two equations ([28]

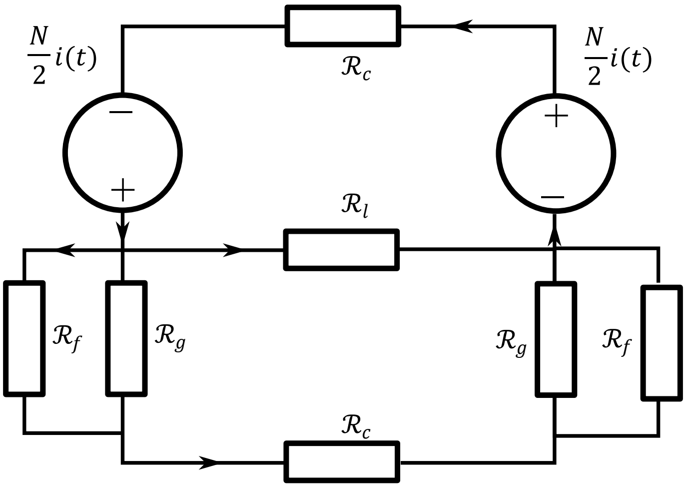

Figure 2.2: Magnetic reluctance network.

Table 2.1: Physical parameter's description

Parameters	**Description**
m [kg]	Mass of the mover
N	Number of coil turns
A [mm^2]	Area of pole
l_c [m]	Magnetic length
μ_r	Relative permeability
$x(t)$ [m]	air gap
f_{mag} [N]	Magnetic force (Reluctance force)
$i(t)$ [A]	Coil current
$v(t)$ [V]	Applied voltage
$L(x)$ [H]	Coil inductance
λ [Wb]	Flux linkage

[29]).

$$f_{mag} = \frac{\phi^2}{\mu_0 A} = -\frac{1}{2}\frac{\partial L(x)}{\partial x} i(t)^2 \tag{2.3}$$

$$\lambda = N\phi = L(x)i(t) \tag{2.4}$$

It should be noted that the inductance $L(x)$ is vital for accurate modeling. A simplified magnetic circuit of EML is shown in Fig. 2.2 where $\mathcal{R}_c, \mathcal{R}_g, \mathcal{R}_f, \mathcal{R}_l$ are reluctance associated with magnetic core, air gap, fringing effects and leakage flux respectively. Using the reluctance network, under the assumption of linear magnetic material or a dominant air gap, inductance is expressed as [29].

$$L(x) = \frac{N^2}{\mathcal{R}_{tot}} \tag{2.5}$$

Where, $\mathcal{R}_{tot}$ is the total reluctance of Fig. 2.2. By solving the network, $\mathcal{R}_{tot}$ is expressed in terms of individual reluctances. Compared to the overall geometry of the EML, if the air gap is sufficiently small, $\mathcal{R}_f$ and $\mathcal{R}_l$ are ignored. The inductance is thus defined as:

$$L(x) = \frac{N^2 \mu_0 A}{2x(t) + \frac{l_c}{\mu_r}} \tag{2.6}$$

$$\text{With } \mathcal{R}_g = \frac{x(t)}{\mu_0 A} \text{ and } \mathcal{R}_c = \frac{l_c}{2\mu_0 \mu_r A}$$

From (2.6), it is observed that inductance is a function of the air gap. This information is later on utilized in Chapter 4 to estimate air gap from inductance.

2.1.1 Approximate Linearized Model

For stabilization of the EML plant, active control is necessary. EML is a non-linear system, however, to apply linear controllers it is linearized about a nominal operating point (x_0, i_0, ϕ_0) as follows. From (2.1),

$$m\ddot{x}(t) = -f_{mag}(x(t), i(t)) + mg \tag{2.7}$$

Taking $x(t) = x_0 + \Delta x(t)$, $i(t) = i_0 + \Delta i(t)$, the magnetic force being a nonlinear relation can be linearly approximated as:

$$f_{mag}\Big(x(t), i(t)\Big) = f_{mag}\Big|_{(x_0,i_0)} + \frac{\partial f_{mag}}{\partial x(t)}\Big|_{(x_0,i_0)} \Delta x(t) + \frac{\partial f_{mag}}{\partial i(t)}\Big|_{(x_0,i_0)} \Delta i(t) \tag{2.8}$$

$$f_{mag}\Big(x(t), i(t)\Big) = f_{mag}\Big|_{(x_0,i_0)} + k_x \Delta x(t) + k_i \Delta i(t) \tag{2.9}$$

Where

$$k_x = \frac{\partial f_{mag}}{\partial x(t)}\Big|_{(x_0,i_0)} = -\frac{1}{2} i_0^2 \frac{\partial^2 L(x)}{\partial x(t)^2}\Big|_{x_0,i_0} = -\frac{4 i_0^2 N^2 \mu_0 A}{(2x(t) + \frac{l_c}{\mu_r})^3} \tag{2.10}$$

$$k_i = \frac{\partial f_{mag}}{\partial i(t)}\Big|_{(x_0,i_0)} = -i_0 \frac{\partial L(x)}{\partial x(t)}\Big|_{(x_0,i_0)} = \frac{2 i_0 N^2 \mu_0 A}{(2x(t) + \frac{l_c}{\mu_r})^2} \tag{2.11}$$

k_x and k_x are called gap coefficient and current coefficient respectively. Putting (2.9) in (2.7)

$$m\ddot{x}(t) = -f_{mag}\Big|_{(x_0,i_0)} + -k_x \Delta x(t) + -k_i \Delta i(t) + mg \tag{2.12}$$

$$m\ddot{\Delta x}(t) = -f_{mag}\Big|_{(x_0,i_0)} + -k_x \Delta x(t) + -k_i \Delta i(t) + mg \tag{2.13}$$

$$m\ddot{\Delta x}(t) = -k_x \Delta x(t) - k_i \Delta i(t) \tag{2.14}$$

Where $f_{mag}\big|_{(x_0,i_0)} = mg$. Using Laplace transform, approximate linear plant model is obtained:

$$G_p(s) = \frac{\Delta X(s)}{\Delta I(s)} = \frac{-k_i}{ms^2 + k_x} \tag{2.15}$$

To model the electrical dynamics, using (2.2) and (2.4):

$$v(t) = i(t)R + \frac{dL(x)i(t)}{dt} \tag{2.16}$$

Letting $L(x) = L_0 + \Delta L(x)$ and $v(t) = v_0 + \Delta v(t)$. $L(x)i(t)$, which is a non-linear term, can be approximated by a linear term as:

$$L(x)i(t) = (L_0 + \Delta L(x))(i_0 + \Delta i(t)) \tag{2.17}$$

$$L(x)i(t) = L_0 i_0 + L_0 \Delta i(t) + \Delta L(x) i_0 + \Delta L(x) \Delta i(t) \tag{2.18}$$

The fourth term, which is too small relatively, can be neglected. Putting (2.18) in (2.16) and substituting $v(t), i(t)$.

$$\begin{aligned}
v_0 + \Delta v(t) &= i_0 R + \Delta i(t) R + \frac{d}{dt}\Big(L_0 i_0 + L_0 \Delta i(t) + \Delta L(x) i_0\Big) \\
v_0 + \Delta v(t) &= i_0 R + \Delta i(t) R + L_0 \frac{d}{dt}\Big(\Delta i(t)\Big) + i_0 \frac{d}{dt}\Big(\Delta L(x)\Big) \\
\Delta v(t) &= \Delta i(t) R + L_0 \frac{d}{dt}\Big(\Delta i(t)\Big) + i_0 \frac{\partial \Delta L(x)}{\partial x(t)} \frac{\partial \Delta x(t)}{\partial t} \\
\Delta v(t) &= \Delta i(t) R + L_0 \Delta \dot{i}(t) - k_i \Delta \dot{x}(t) \qquad (2.19)
\end{aligned}$$

Where $v_0 = i_0 R$ and $L_0 = \frac{N^2 \mu_0 A}{2x_0 + \frac{l_c}{\mu_r}}$ is nominal inductance. Using Laplace transform, the electrical dynamics are represented as:

$$\Delta I(s) = \frac{1}{sL_0 + R} \Delta V(s) + \frac{s k_i}{sL_0 + R} \Delta X(s) \tag{2.20}$$

Using (2.15) and (2.20), complete plant dynamics are represented as a block diagram in Fig. 2.3. In order to apply modern control theories, it is suitable to obtain state space representations of the linearized plant model. If $\Delta i(t)$ is assumed as an input, the second order state space representation of the EML plant by taking $\Delta x(t)$ and $\Delta \dot{x}(t)$ as states is shown below:

$$\begin{bmatrix} \Delta \dot{x}(t) \\ \Delta \ddot{x}(t) \end{bmatrix} = \begin{bmatrix} 0 & 1 \\ -\frac{k_x}{m} & 0 \end{bmatrix} \begin{bmatrix} \Delta x(t) \\ \Delta \dot{x}(t) \end{bmatrix} + \begin{bmatrix} 0 \\ -\frac{k_i}{m} \end{bmatrix} \Delta i(t) \tag{2.21}$$

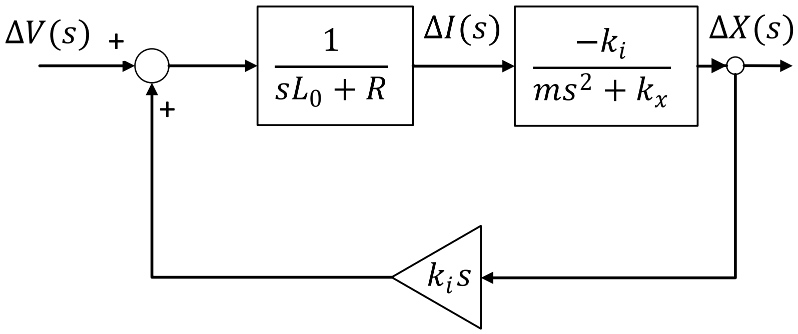

Figure 2.3: Linearized EML plant model.

Where $\mathbf{A_2} = \begin{bmatrix} 0 & 1 \\ -\frac{k_x}{m} & 0 \end{bmatrix}$, $\mathbf{X_2} = \begin{bmatrix} \Delta x(t) \\ \Delta \dot{x}(t) \end{bmatrix}$ and $\mathbf{B_2} = \begin{bmatrix} 0 \\ -\frac{k_i}{m} \end{bmatrix}$.
The output matrix is determined based on the how many states sensors can measure. The second order state space representation is used later on in Chapter 3 for controller design and in Chapter 4 for observer design. Furthermore, third order state space representation is next given since it shall be used for design of zero power control in Chapter 5. In this case, the electrical dynamics are included in the model. Using (2.14) and (2.19), and using $\Delta x(t)$, $\Delta \dot{x}(t)$ and $\Delta i(t)$ as states, we have:

$$\begin{bmatrix} \Delta \dot{x}(t) \\ \Delta \ddot{x}(t) \\ \Delta \dot{i}(t) \end{bmatrix} = \begin{bmatrix} 0 & 1 & 0 \\ -\frac{k_x}{m} & 0 & -\frac{k_i}{m} \\ 0 & \frac{k_i}{L_0} & -\frac{R}{L_0} \end{bmatrix} \begin{bmatrix} \Delta x(t) \\ \Delta \dot{x}(t) \\ \Delta i(t) \end{bmatrix} + \begin{bmatrix} 0 \\ 0 \\ \frac{1}{L_0} \end{bmatrix} \Delta v(t) \tag{2.22}$$

Where $\mathbf{A_3} = \begin{bmatrix} 0 & 1 & 0 \\ -\frac{k_x}{m} & 0 & -\frac{k_i}{m} \\ 0 & \frac{k_i}{L_0} & -\frac{R}{L_0} \end{bmatrix}$, $\mathbf{x_3} = \begin{bmatrix} \Delta x(t) \\ \Delta \dot{x}(t) \\ \Delta i(t) \end{bmatrix}$ and $\mathbf{B_2} = \begin{bmatrix} 0 \\ 0 \\ \frac{1}{L_0} \end{bmatrix}$.

2.2 Numerical Model using CAD

A numerical simulation is carried out for the electromagnet shown in Fig. 2.4. Corresponding core and winding dimensions are given in Fig. 2.5. Number of approximate winding turns are 200 each side, so total turns $N \approx 400$. The software used is JMAG. The simulation includes sweeping the air gap length from 0.1[mm] to 12[mm] at a constant dc current of 0.2[A]. The purpose is to obtain flux linkage of coils at different gap lengths and calculate inductance.

The inductance profile obtained via numerical simulation is shown in Fig. 2.6. For gap length till 1[mm], the analytical model and numerical model inductances coincide since

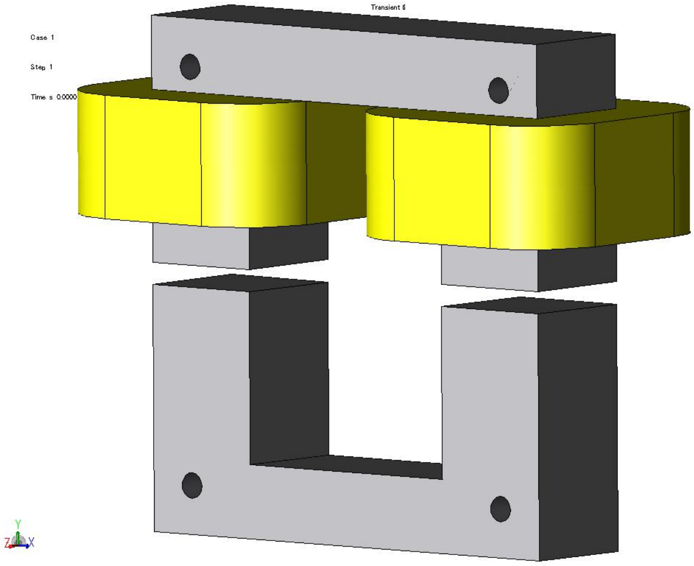

Figure 2.4: Electromagnetic levitation module used for numerical simulation.

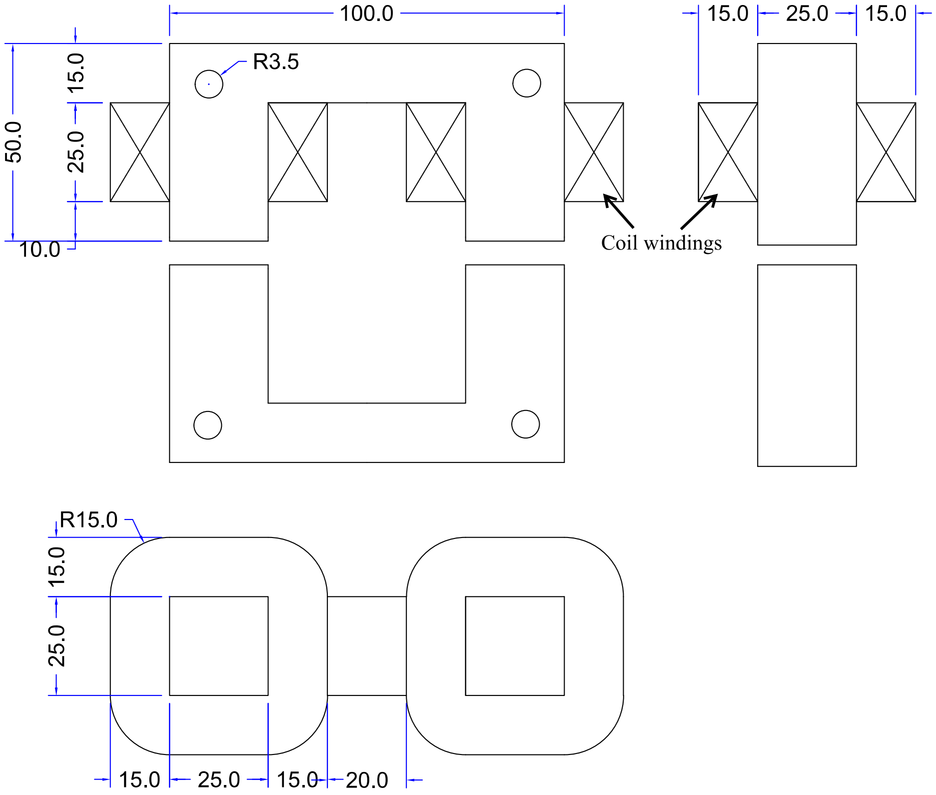

Figure 2.5: Core dimensions of the electromagnetic levitation plant.

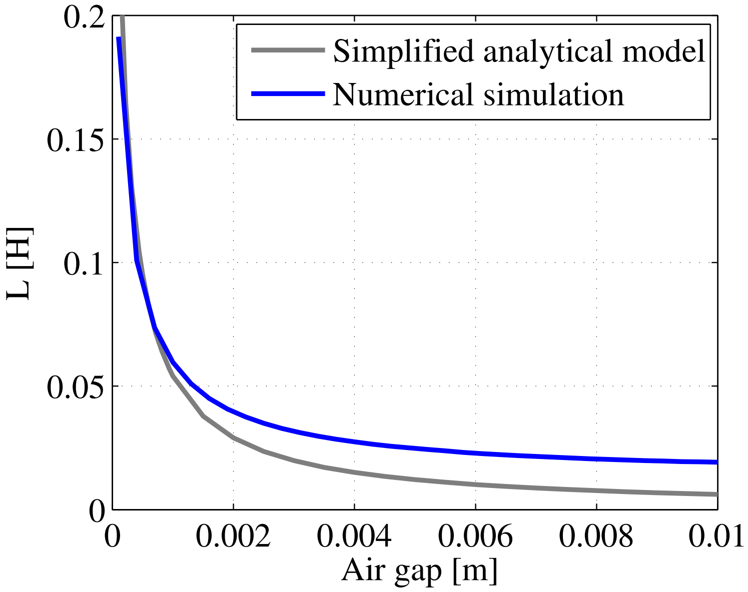

Figure 2.6: Inductance vs air gap profile: Comparison between numerical simulation and simplified analytical model.

the approximation of constant flux in air gap and negligible fringing and leakage is satisfied. But for case when gap length increases, the simplified analytical model assumption fails and the inductance profiles deviate from one another, with numerical model being the real case. The above claim is further supported by flux line illustrations shown in Fig. 2.7. For similar conditions in both cases, the one with gap length 8 [mm] has significant leakage flux lines. This exercise is a proof that the magnetic circuit relations derived in previous section become invalid at large air gap range. For this reason, the experimental model is used for modeling the magnetic link as explained in next section.

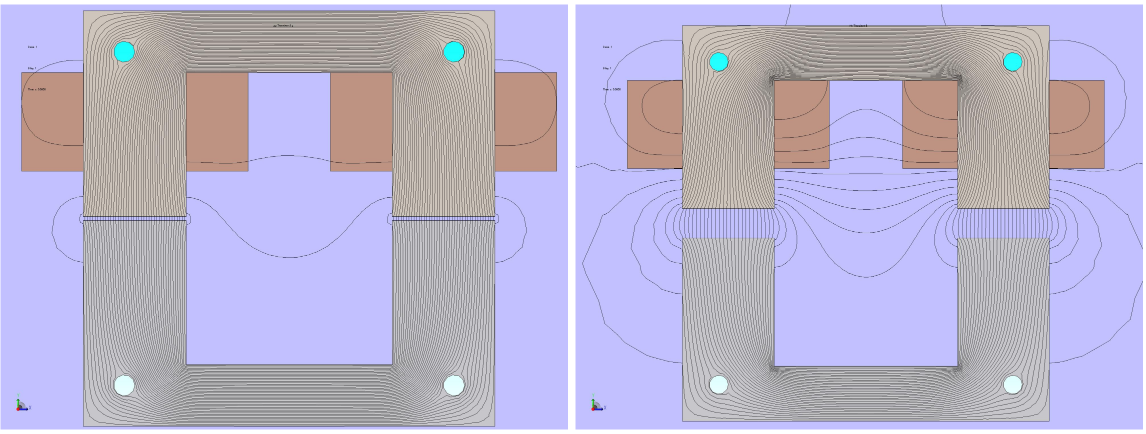
(a) (b)

Figure 2.7: Fringing and leakage represented by flux lines for 2D simulation: (a) At 1[mm], negligible. (b) At 8[mm], significantly large.

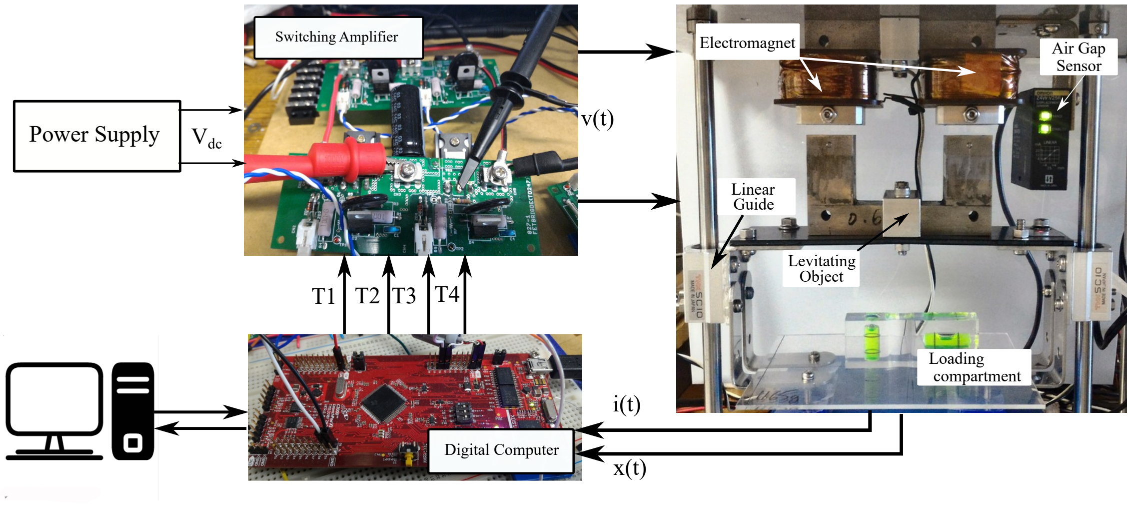

Figure 2.8: Experimental Setup.

2.3 Modeling of Experimental Test Bench

A test bench has been designed for experimental verification of the concepts and methods proposed in successive chapters. The entire setup is shown in Fig. 2.8. The EML system consists of two C-cores. The upper one is fixed while the lower one moves in only vertical direction. Other degrees of freedom (pitch and yaw) are restricted by linear bearings. The fixed core has windings on both of its poles connected in series. Current sensor used is LEM LTSR 6-NP with a sensitivity of 206 [mV/A]. Air gap sensor, Omron Z4W-V25R LED Displacement Sensor, is also used to log measured air gap for comparison purposes. Detailed specifications of the sensors can be found in respective data sheets (1)(2). The controller, sensorless methods etc are all implemented in Texas Instrument's micro-controller TMS320F28377S. The Micro-controller outputs four gate signals $T1, T2, T3, T4$ used to drive the switching power amplifier that drives the electromagnetic coil of the plant.

The electrical and mechanical parameters such as coil resistance R and carrier mass m are easily measured by relevant instruments. A significant problem is the modeling of the magnetic circuit. Linear approximation in magnetic circuit (Fig. 2.2) is valid for small values of air gap, where leakage and fringing effects are negligible. Since our operation is around $8\sim10$[mm], it was shown in previous section that linear magnetic circuit cannot be used. Parameters such coil turns N, core magnetic path l_c can still be measured. But exact effective pole area at large air gap is difficult to measure remains problematic. Therefore, author is of the view that inductance $L(x)$ profile has the answers to all modeling issues. If $L(x)$ profile can be obtained experimentally (or by numerical simulation as was done in previous section), all modeling requirements of magnetic domain are fulfilled. This evident from the use of $L(x)$, $\frac{\partial L(x)}{\partial x}$ and $\frac{\partial^2 L(x)}{\partial x^2}$ in calculation of force f_{mag}, current coefficient

---

[1] http://www.lem.com/docs/products/ltsr%206-np.pdf

[2] http://www.ia.omron.com/data_pdf/cat/z4w-v_e217-e1_3_1_csm1402.pdf

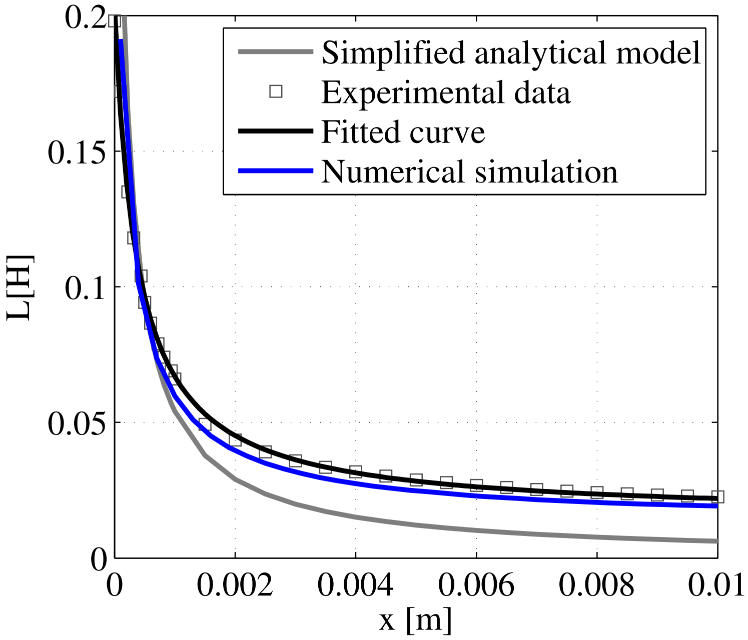

Figure 2.9: Inductance vs air gap profile.

k_i and gap coefficient k_x.

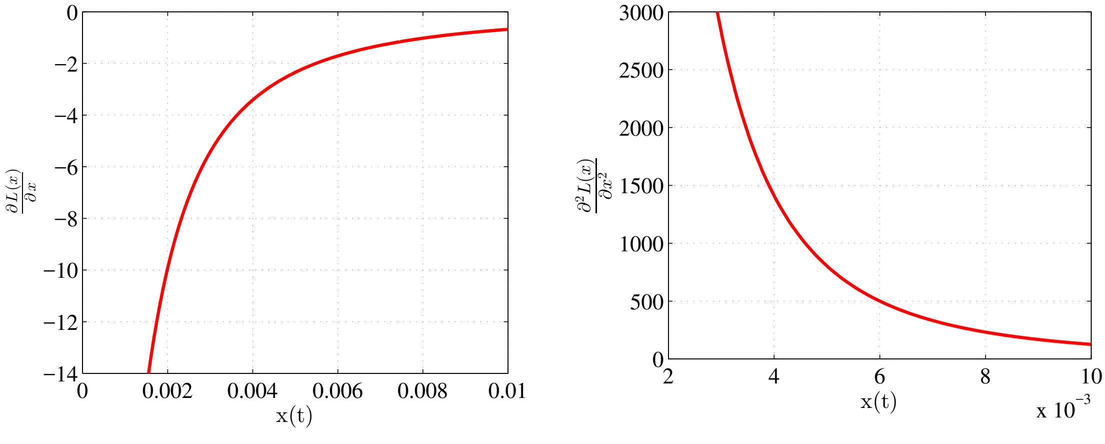

(a) (b)

Figure 2.10: Inductance profile high order derivatives. (a) $\frac{\partial L(x)}{\partial x}$. (b) $\frac{\partial^2 L(x)}{\partial x^2}$.

With the above discussion in mind, a data base of inductance at different air gap lengths ranging from 0 to 12[mm] is collected by first fixing the gap length at known position, exiting the coil by switching voltage and using sensorless method (Chapter 4) to calculate inductance. Simultaneously, an LCR meter is used to verify the calculated inductance. A curve fitting tool in Matlab is used to represent the data base as a rational

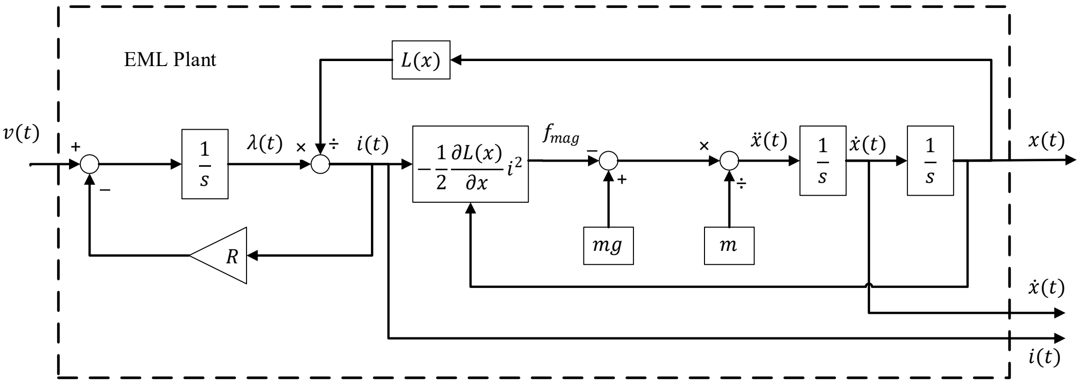

Figure 2.11: Electromagnetic levitation plant schematic used in numerical case studies.

polynomial as:

$$L(x) = \frac{p_1 x + q_2}{x + q_1} \tag{2.23}$$

Where $p_1 = 0.0151$, $p_2 = 9.267 \times 10^{-3}$ and $q_1 = 0.0008391$. A manipulated form $x_{est} = f(L_{est})$ of same expression is used in Chapter 4 to calculate air gap x_{est} from estimated inductance L_{est} in the proposed sensorless method. Since (2.23) is continuous and rational, $\frac{\partial L(x)}{\partial x}$ and $\frac{\partial^2 L(x)}{\partial x^2}$ are easily calculated for a particular air gap length. Figure 2.9 shows the inductance profile. As stated before, it is evident that linear magnetic circuit modeling fails are large air gap. Higher order derivatives for inductance profile used for calculation of k_i and k_x are also shown in Fig. 2.10.

For all control related calculations in the following chapters, the magnetic domain related parameters used are obtained from these profiles and the EML plant used is shown in Fig. 2.11. It can be observed that the magnetic link between electrical and mechanical domain is represented by just inductance and its derivative profiles.

Chapter 3

Design of Controllers for Electromagnetic Levitation

Electromagnetic Levitation (EML) is inherently an unstable system. This can be observed from the characteristic equation of the plant expressed in (2.15). The characteristic equation in this case has one pole in the right hand side (RHS) of the imaginary axis as shown below:

$$P(s) = ms^2 + k_x \tag{3.1}$$

Since $k_x < 0$, the poles are real with one being unstable. This requires active control at all times. A simple control system for EML is shown in Fig. . Gap sensor measures the air gap and feeds it to the controller, which according to control law generates output voltage. Voltage is feed to the coil via power amplifier. The resulting current in the coil generates magnetic force and is accordingly controlled to maintain a stable levitation. In this chapter, starting from the simple and conventional control, different control laws are designed and experimentally verified on our system.

3.1 Proportional-Derivative(PD) Gap Control

The first objective in designing control system for EML is stabilization. Once stabilization is achieved, performance characteristics can be dealt with later on. In EML system, since it is a contact less suspension, there is no damping in the system. In order to add artificial damping, derivative (D) term is used. Proportional (P) term is added to control the speed of step response. The controller transfer function used is:

$$PD(s) = k_P + \frac{k_D s}{\tau_D s + 1} \tag{3.2}$$

Since the air gap sensor output is noisy, approximate derivative is used. The PD controlled EML system schematic is shown in Fig. 3.1. The PD gains are placed in the feedback

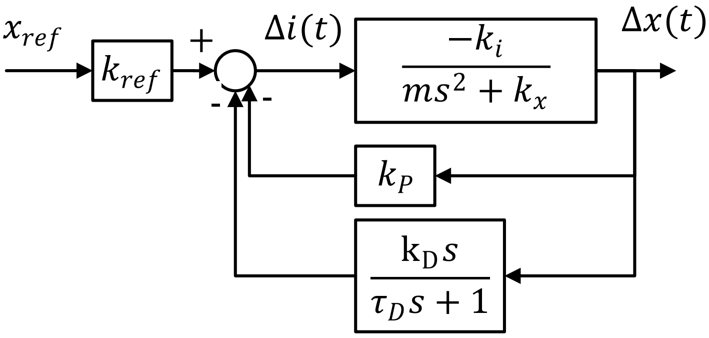

Figure 3.1: Proportional-Derivative (PD) control loop

path so that later on a second degree of freedom (Integral (I) term) can be added without considerably changing stabilizing PD gains. The closed loop transfer function is then calculated as:

$$G_{CL}(s) = \frac{-k_i k_{ref}}{m\tau_D s^3 + ms^2 + (k_x\tau_D - k_i k_P \tau_D - k_i k_D)s + k_x - k_i k_P} \tag{3.3}$$

Equating the characteristic equation to a third order polynomial given in (3.4) , the gains are calculated as shown below:

$$Xtic_3(s) = a_3 s^3 + a_2 s^2 + a_1 s + a_0 \tag{3.4}$$

$$\begin{aligned} k_P &= \frac{a_0 m\tau_D - k_x}{-k_i} \\ k_D &= \frac{a_1 m\tau_D - k_x\tau_D + k_i k_P \tau_D}{-k_i} \\ \tau_D &= \frac{1}{a_2} \end{aligned} \tag{3.5}$$

The k_{ref} is chosen to be inverse of the dc gain for feedback loop.

3.1.1 Manabe's Coefficient Diagram Method

We use Manabe's coefficient method [27] to decide coefficients of the desired characteristic polynomial. According to this method, the coefficient are decided based on the following conditions:

$$\gamma_i = \frac{a_i^2}{a_{i+1}a_{i-1}} \qquad \text{for } i = 1, 2, \dots n-1 \tag{3.6}$$

$$\tau = \frac{a_1}{a_0} \tag{3.7}$$

$$\gamma_i^* = \frac{1}{\gamma_{i+1}} + \frac{1}{\gamma_{i-1}} \qquad \text{Where } \gamma_n, \gamma_0 = \infty \tag{3.8}$$

Where γ_i is the stability index, γ_i^* is the stability limit and τ is use to specify the desired time response. According to Manabe's work in [27], the polynomial results in a stable response whose stability indexes are given as:

$$\gamma_1 = 2.5$$
$$\gamma_i = 2 \quad \text{for } i >= 2$$

Using Manabe's method, the coefficients are calculated as:

$$a_1 = a_0\tau \tag{3.9}$$

$$a_2 = \frac{a_0\tau^2}{\gamma_1} \tag{3.10}$$

$$a_3 = \frac{a_0\tau^3}{\gamma_1^2\gamma_2} \tag{3.11}$$

Thus for an nth order polynomial, all coefficients are expressed in terms of a_0, γ_i and τ as shown below:

$$a_i = \frac{a_0\tau^i}{(\gamma_{i-1}\gamma_{i-2}^2 \cdots \gamma_1^{i-1})} \qquad \text{Where } i = 2\dots n \tag{3.12}$$

In general case, $a_n = 1$ allowing us to evaluate a_0 as well. The remaining tuning parameters are reduced to just τ.

3.1.2 PD Control: Simulation verification

In order to verify the designed gains, numerical simulation is carried out in Simulink/Matlab. Table 3.1 shows the numerical values of the parameters used. It should be noted here, that the experimental values, obtained in Chapter 1, of plant characteristic coefficients k_i and k_x are used in controller design. For $\tau = 0.05$[sec], the controller gains calculated using (3.5) are:

$$k_P = -773[\text{A/m}] \qquad k_D = -9.68[\text{As/m}] \qquad \tau_D = 0.01[\text{sec}]$$

Table 3.1: Parameter values in simulations/experiments for PD control

Parameters	**Value**	**Parameters**	**Value**
m [kg]	1.165	N	400
V_{dc} [V]	45	T_{pwm} [sec]	2×10^{-3}
R [Ω]	1.7	x_0 [m]	8×10^{-3}
i_0 [A]	4.7	L_0 [H]	24.1×10^{-3}
k_i [N/A]	4.84	k_x [N/m]	-2.59×10^3

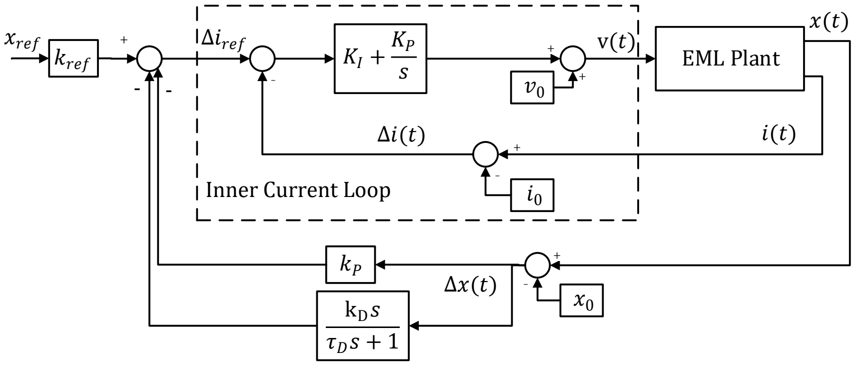

Figure 3.2: PD control block diagram used in simulation.

The schematic for simulation is shown in Fig. 3.2. An inner PI current control is also applied since input to the plant is voltage. It is important to note that the closed loop bandwidth f_c for current controller is kept significantly larger than the closed loop bandwidth f_g for gap controller. In design, this is achieved by keeping $\tau \approx\ 10\tau_c$. Simulation results for PD gap controller are shown in Fig 3.3. The step response for the specified $\tau = 0.05$

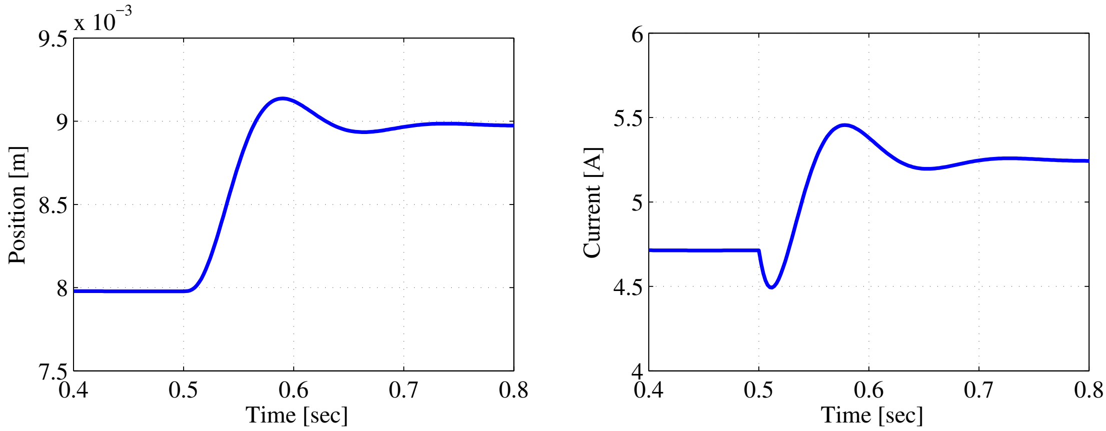

(a)

(b)

Figure 3.3: PD controller simulation results for step command: (a) Position. (b) Time period average Current.

and stability indexes is as expected. To analyze the effect of changing design parameters,

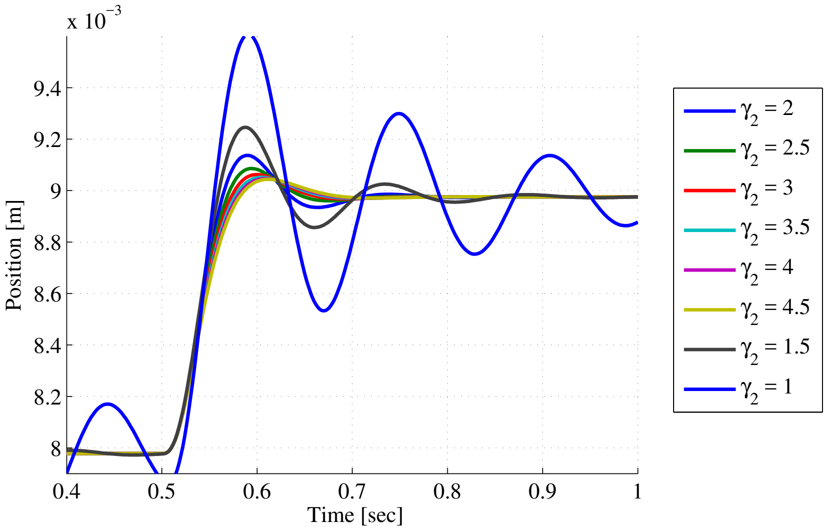

Figure 3.4: PD controller step response with different γ_2

the step responses for different values of γ_2 are given in Fig. 3.4. This is expected since by increasing the stability index, the system moves towards stability. Physical interpretation of this trend it given to the fact that by varying γ_2, the τ_D changes from $0.02 \sim 0.0044$. That means, the derivative filter's added delay gets reduced and consequently the system response has increased damping. For values $\gamma_2 > 2.5$, k_P and k_D do not vary much. Using (3.8), stability limit for γ_2 given as $\gamma_2^* = \frac{1}{\infty} + \frac{1}{2.5} = 0.4$ corresponds to $\tau_D = 0.05$ and $k_D = 0$ which physically mean no artificial damping. For values slightly larger than γ_2^*, for instance $\gamma_2 = 1$, the results is oscillatory with $\tau_D = 0.02$. It is important to determine the maximum value of τ_D that can be used without going into instability since later in chapter 4, it is an important parameter in reducing noise in velocity signal obtained from estimated air gap.

3.1.3 PD control: Experimental Verification

In experimental verification, switching amplifier is used to convert voltage output signal of controller into pulses of time period $T_{pwm} = 2 \times 10^{-3}$[sec]. This puts a limitation on the minimum control period that can be used. Although, our hardware supports smaller T_{pwm}, but the choice of T_{pwm} depends on the sensorless gap detection algorithm which is described later in Chapter 4. In order to maintain consistency with the control laws applied for sensorless air gap detection, we choose to keep $T_{pwm} = 2 \times 10^{-3}$[sec] in this Chapter. The current controller is designed while maintaining that $T_{pwm} = 10\% T_{rc}$, and $T_{rc} = 2.2\tau_c$ where T_{rc} is the rise time for the current response. The gains for current controller are tuned to be $K_P = 5$ and $K_I = 500$. With inner current control designed, the gap control gains used are the same as one designed in this section, with slight additional tuning. The experimental results for PD controller are given in Fig. 3.5.

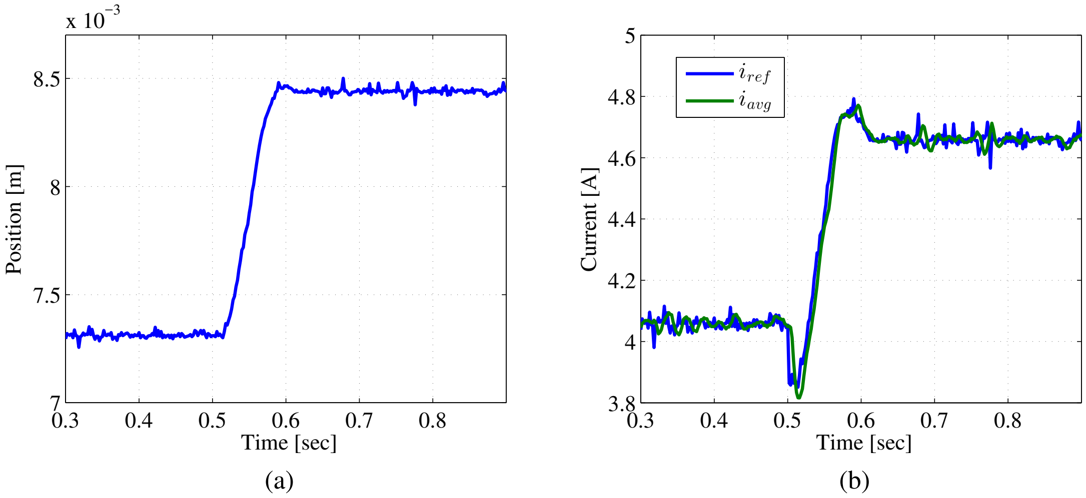

Figure 3.5: PD controller experimental results (a) Position. (b) Inner loop current tracking.

Since the experimental test bench has linear guides that limit the motion in only z-direction, they add slight additional damping. As a result, the step response shown in 3.5(a) shows no overshoot. Furthermore, Fig. 3.5(b) shows that current follows the reference current accurately, thus it can be inferred that closed loop current control does not significantly affect the outer gap loop. These results only depict stabilization which is the first step in EML control. The designed controller in this section is used later on with sensorless air gap detection methods in chapter 4. It should be noted that there is no exact position control. The k_{ref} is set by trial and error until a suitable step of 1[mm] is obtained.

3.2 Three-States Feedback Control

The motivation behind design of state feedback control is that it forms the basis of the more advanced control techniques that can be applied. For instance, in chapter 5, zero power control is introduced, which is in fact state feedback control with additional integral gain for current. Similarly, for position tracking, prior to position integral control, an inner state feedback is necessary to achieve stabilization. With the above in mind, this step is vital for moving forward in control application for EML system.

A three state representation of EML plant was derived in chapter 2. The expression is repeated here for convenience:

$$\begin{bmatrix} \Delta\dot{x}(t) \\ \Delta\ddot{x}(t) \\ \Delta\dot{i}(t) \end{bmatrix} = \begin{bmatrix} 0 & 1 & 0 \\ -\frac{k_x}{m} & 0 & -\frac{k_i}{m} \\ 0 & \frac{k_i}{L_0} & -\frac{R}{L_0} \end{bmatrix} \begin{bmatrix} \Delta x(t) \\ \Delta\dot{x}(t) \\ \Delta i(t) \end{bmatrix} + \begin{bmatrix} 0 \\ 0 \\ \frac{1}{L_0} \end{bmatrix} \Delta v(t) \tag{3.13}$$

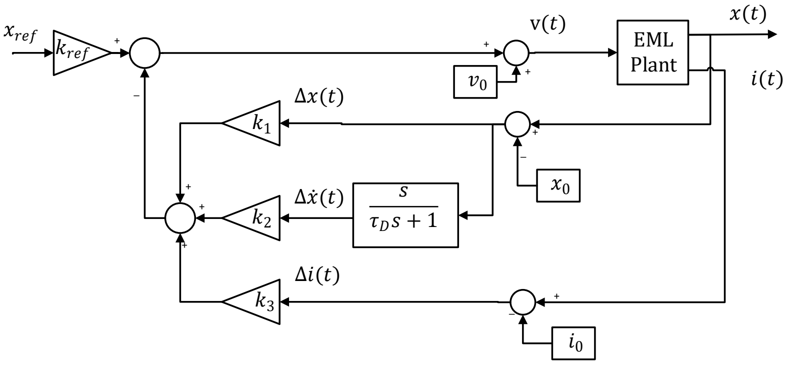

Figure 3.6: State feedback schematic diagram.

Where $\mathbf{A_3} = \begin{bmatrix} 0 & 1 & 0 \\ -\frac{k_x}{m} & 0 & -\frac{k_i}{m} \\ 0 & \frac{k_i}{L_0} & -\frac{R}{L_0} \end{bmatrix}$, $\mathbf{x_3} = \begin{bmatrix} \Delta x(t) \\ \Delta \dot{x}(t) \\ \Delta i(t) \end{bmatrix}$ and $\mathbf{B_2} = \begin{bmatrix} 0 \\ 0 \\ \frac{1}{L_0} \end{bmatrix}$.

The state feedback schematic is shown in Fig. 3.6. Proceeding forward with state feedback controller, the input to the plant is given as:

$$\Delta v(t) = -\mathbf{K}\mathbf{x_3} + k_{ref} x_{ref} \tag{3.14}$$

Where $\mathbf{K} = \begin{bmatrix} k_1 & k_2 & k_3 \end{bmatrix}$ and k_{ref} is used to adjust dc gain. The closed loop system thus obtained is:

$$\begin{bmatrix} \Delta \dot{x}(t) \\ \Delta \ddot{x}(t) \\ \Delta \dot{i}(t) \end{bmatrix} = \begin{bmatrix} 0 & 1 & 0 \\ -\dfrac{k_x}{m} & 0 & -\dfrac{k_i}{m} \\ -\dfrac{k_1}{L_0} & \dfrac{k_i}{L_0} - \dfrac{k_2}{L_0} & -\dfrac{R}{L_0} - \dfrac{k_3}{L_0} \end{bmatrix} \begin{bmatrix} \Delta x(t) \\ \Delta \dot{x}(t) \\ \Delta i(t) \end{bmatrix} + \begin{bmatrix} 0 \\ 0 \\ \frac{k_{ref}}{L_0} \end{bmatrix} x_{ref} \tag{3.15}$$

The characteristic equation of (3.15) is calculated as:

$$s^3 + \left(\frac{R}{L_0} + \frac{k_3}{L_0}\right)s^2 + \left(\frac{k_i^2}{mL_0} - \frac{k_i k_2}{mL_0} + \frac{k_x}{m}\right)s + \left(\frac{k_x R}{mL_0} + \frac{k_x k_3}{mL_0} - \frac{k_i K_1}{mL_0}\right) = 0 \tag{3.16}$$

Manabe's 3rd order polynomial is used to calculate the controller gains, represented as:

$$s^3 + \frac{\gamma_1 \gamma_2}{\tau_3} s^2 + \frac{\gamma_1^2 \gamma_2}{\tau_3^2} s + \frac{\gamma_1^2 \gamma_2}{\tau_3^3} = 0 \tag{3.17}$$

Where τ_3 is the time constant used to tune controller speed, $\gamma_1 = 2.5$ and $\gamma_2 = 2$. The state feedback gains are thus calculated by equating (3.16) and (3.17):

$$k_1 = \frac{1}{k_i}\Big(k_x R + k_x k_3 - \frac{\gamma_1^2\gamma_2}{\tau_3^3} m L_0\Big) \tag{3.18}$$

$$k_2 = \frac{mL_0}{k_i}\Big(\frac{k_i^2}{mL_0} + \frac{k_x}{m} - \frac{\gamma_1^2\gamma_2}{\tau_3^2}\Big) \tag{3.19}$$

$$k_3 = L_0\Big(\frac{\gamma_1\gamma_2}{\tau_3} - \frac{R}{L_0}\Big) \tag{3.20}$$

Since this is centralized control, bandwidth separation of air gap control and current control need not to be cared for. The controller time constant is set to $\tau_3 = 0.035$[sec] by tuning. The resulting gains are:

$$k_1 = -3539[\text{V/m}] \qquad k_2 = -67.3[\text{Vs/m}] \qquad k_3 = 1.75[\text{V/A}]$$

In calculation of gains, the plant parameters k_i and k_x used are the same as in previous section shown in Table. 3.1. Simulation on non-linear plant is carried out and the results are shown in Fig. 3.7. Also experimental results are shown in Fig. 3.8. The results are similar to our expectations. However, velocity signal has considerable noise since it was generated by first order derivative. Careful design of state observer can produce a noise free velocity signal. This is done in chapter 4 in case when estimated air gap signal from sensorless method is used as feedback. Later, in chapter 5, design of zero power control is also facilitated by using similar procedure for gain calculation of an inner loop state feedback controller.

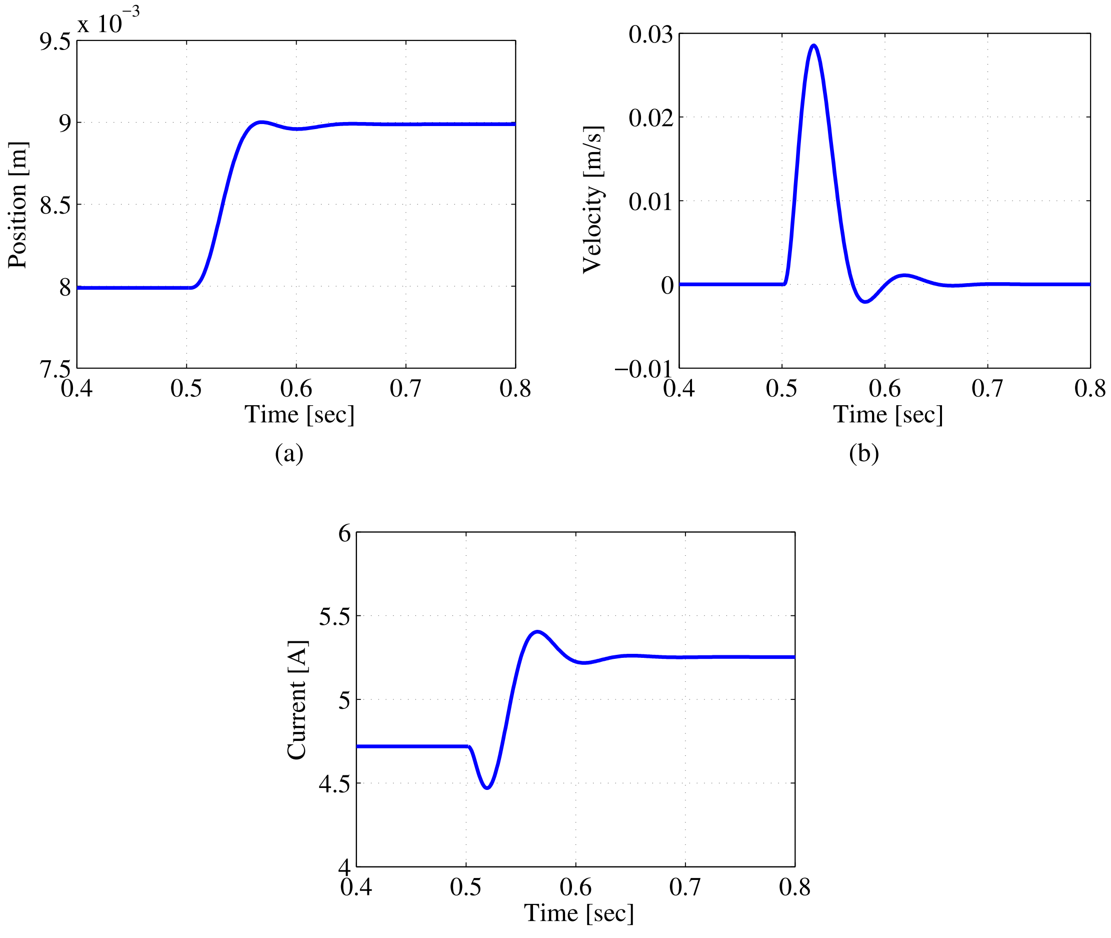

(a)

(b)

(c)

Figure 3.7: Experimental results for state feedback controller: (a) Position. (b) Velocity. (c) Time period average current.

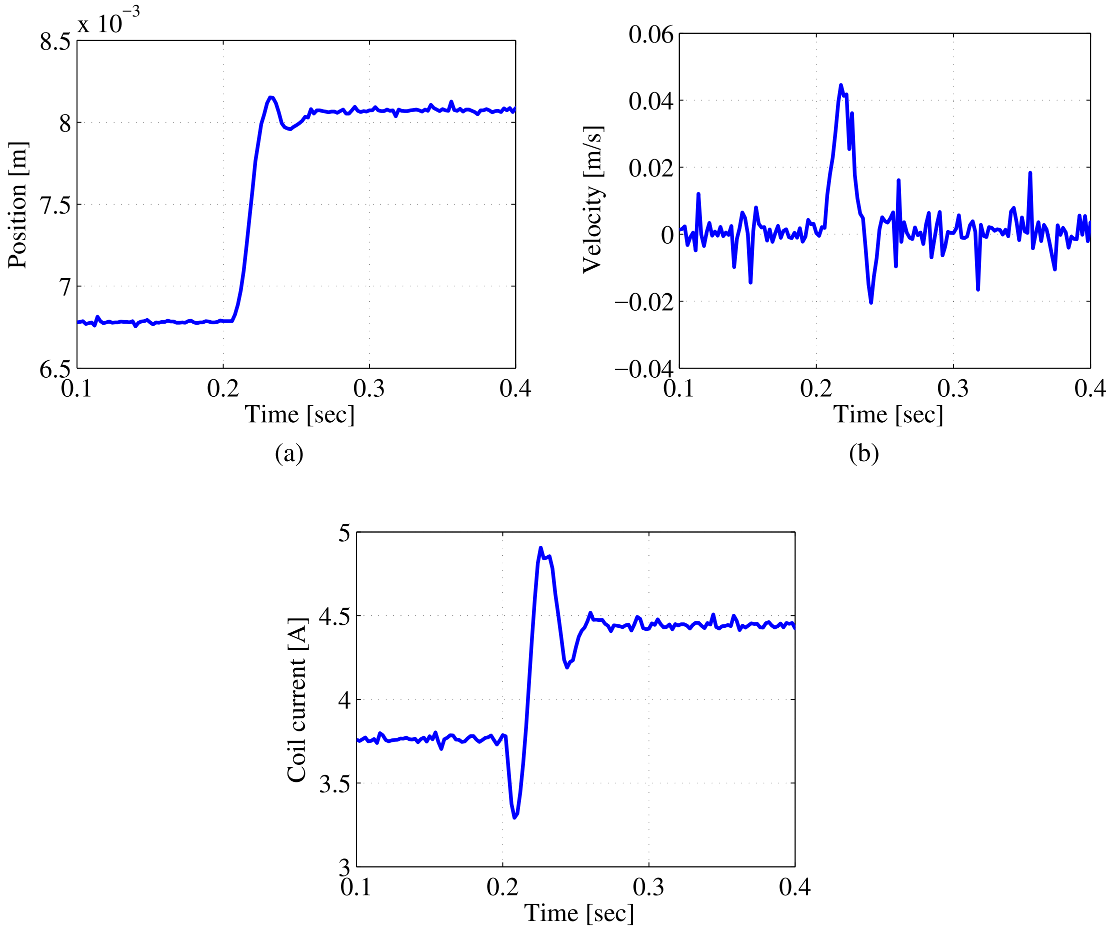

(a)

(b)

(c)

Figure 3.8: Experimental results for state feedback controller: (a) Position. (b) Velocity. (c) Time period average Current.

Chapter 4

Sensorless Air Gap Detection Algorithm for Electromagnetic Levitation

Sensorless or self-sensing EML uses the current and voltage measurements as a virtual displacement sensor. The basics of sensorless EML is to estimate the system inductance by signal processing the current and voltage measurements and using accurate system model to detect air gap from the estimated inductance. A comprehensive background is given in Chapter 1 about the types of sensorless methods. Here, we shall discuss the method in which a deliberate voltage perturbation is injected into the system and the resulting coil current ripple is measured and passed through signal processing filters to obtain an estimate of air gap. It was first demonstrated by Okada [14]. This perturbation method has been researched for the past two decades. Instead of employing Band Pass Filters (BFP), recent advances in the power electronics and low cost high speed Analog to Digital Converters (ADCs) allow us to directly measure the current-ripple slope and use it to output an air gap signal. Unlike previous works in current-ripple slope methods, we have proposed a method that overcomes the dependence of detection accuracy on duty ratio variation.

4.1 Proposed Air Gap Detection Method

Due to the industrial wide spread of switching amplifiers, they are used as source of high frequency injection as well. Figure 4.1 shows a typical switching amplifier which is employed in our experiments. The switching amplifier generates a pulsating voltage given as:

$$v(t) = \begin{cases} V_{dc} & 0 < t < \alpha T_{pwm} \\ -V_{dc} & \alpha T_{pwm} < t < T_{pwm} \end{cases} \tag{4.1}$$

In response to (4.1), electromagnetic coil current response is shown in Fig. 4.2. Information about inductance is embedded in the current-ripple which is exploited to detect

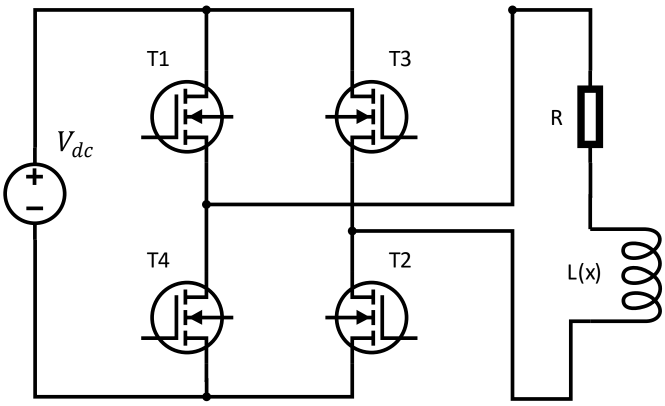

Figure 4.1: Switching amplifier and gate signals configuration

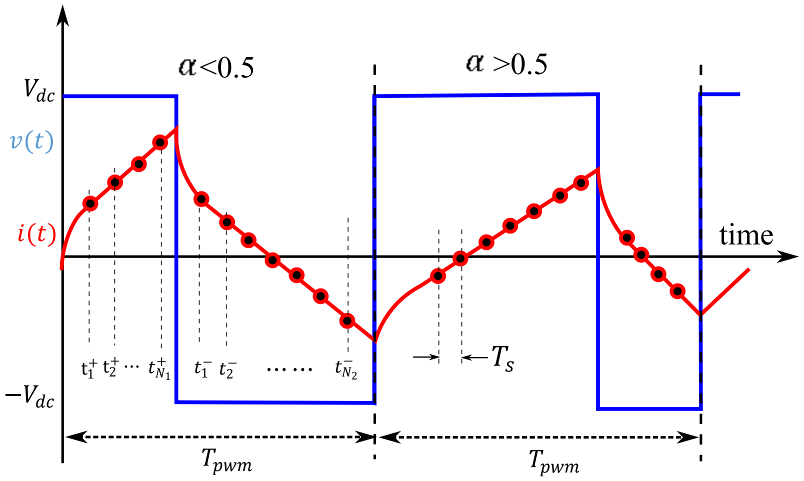

Figure 4.2: Timing diagram for single slope detection

the air gap. Using (2.2) and (2.4) we proceed as:

$$v(t) = i(t)R + \frac{dL(x)i(t)}{dt} \tag{4.2}$$

$$v(t) = i(t)R + L(x)\frac{di(t)}{dt} + i(t)\frac{\partial L(x)}{\partial x}\frac{dx(t)}{dt} \tag{4.3}$$

The dynamic frequency range of a levitating vehicle is much less than the switching frequency of the amplifier. In magnetic bearings the operational range is $0.1 \sim 1$mm and sensitivity of inductance $\frac{\partial L(x)}{\partial x}$ is high. Unlike that, at $8 \sim 10$mm $\frac{\partial L(x)}{\partial x}$ is quite low as shown in Fig. 2.10(a). Furthermore $\frac{dx(t)}{dt}$ is around $|0.05|$m/s in our experiment. Thus, third term in (4.3) is negligible and is ignored. Integrating modified (4.3) from t_1 to t_{N_1}

(Fig. 4.2) gives:

$$\int_{t_1}^{t_{N_1}} v(t)dt = \int_{t_1}^{t_{N_1}} i(t)Rdt + \int_{t_1}^{t_{N_1}} L(x)di(t) \tag{4.4}$$

$$L(x)\frac{i(t_{N_1}) - i(t_1)}{t_{N_1} - t_1} = V_{dc} - \frac{1}{t_{N_1} - t_1}\int_{t_1}^{t_{N_1}} i(t)Rdt \tag{4.5}$$

Let $\frac{\Delta i^+}{\Delta t} = \frac{i(t_{N_1})-i(t_1)}{t_{N_1}-t_1}$ and $\bar{i}^+ = \frac{1}{t_{N_1}-t_1}\int_{t_1}^{t_{N_1}} i(t)dt$.

$$L_{est}^+ = \frac{V_{dc} - \bar{i}^+ R}{\frac{\Delta i^+}{\Delta t}} \tag{4.6}$$

Where, $L(x)$ is replaced by estimated inductance L_{est}^+. Within a switching period, only two measurements of the rising part of current-ripple are sufficient to calculate its approximate slope $\frac{\Delta i^+}{\Delta t}$. But due to measurement noise, the slope calculation has large variance. To provide sufficient accuracy, multiple current samples are used and current-ripple is modeled as a straight line by employing the Least Squares Method (LSM). This approximation of the current-ripple as a straight line is valid only if the time constant of LR circuit is sufficiently larger than the switching period T_{pwm} so that the slope remains nearly constant. The sampled data and the estimated current-ripple slope using LMS is given as:

$$\mathbf{i}^+ = [i_1^+, i_2^+, i_3^+, \cdots i_{N_1}^+] \qquad \mathbf{t}^+ = [t_1^+, t_2^+, t_3^+ \cdots t_{N_1}^+]$$
$$\frac{\Delta i^+}{\Delta t} = \frac{\sum_{k=1}^{N_1}(i_k^+ - \bar{i}^+)(t_k^+ - \bar{t})}{\sum_{k=1}^{N_1}(t_k^+ - \bar{t})^2} \tag{4.7}$$

Where $\bar{t}$ is the mean of the array $\mathbf{t}^+$.The same procedure can be applied to obtain the inductance by negative slope calculation.

$$L_{est}^- = \frac{-V_{dc} - \bar{i}^- R}{\frac{\Delta i^-}{\Delta t}} \tag{4.8}$$

Once the inductance is correctly calculated, an experimentally obtained data set, fitted to a rational polynomial $x_{est} = f(L)$, between air gap and inductance is used to obtain the estimated air gap signal.

4.1.1 Single Slope Detection Algorithm

Since the duty ratio α continuously varies when the control law is being executed, the time duration of positive and negative slope changes. Consequently, the number of corresponding current samples (N_1 and N_2) vary as well. To ensure a threshold on maximum

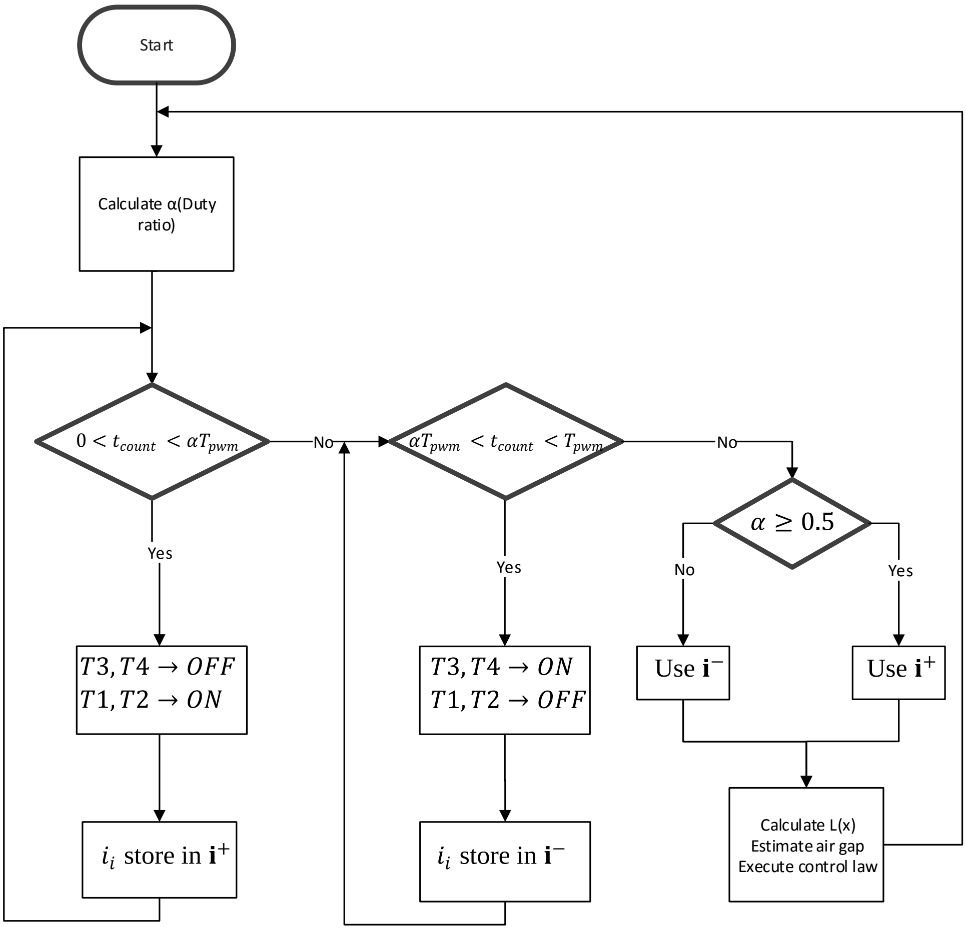

Figure 4.3: Flow of single slope detection algorithm

error in slope calculation, number of current samples should not be reduced below a specific number. Otherwise slope estimation is be erroneous. To prevent that, in previous works α is restricted to $0.25 \sim 0.75$, limiting the available DC voltage. Having 100% of the DC bus voltage allows for a larger range of control effort and improved current control.

The total number of current samples remain constant in a switching period. For $\alpha > 0.5$, rising duration of current-ripple is more than the falling duration and vice versa for $\alpha < 0.5$ as shown in Fig. 4.2. Therefore exploiting the fact that it depends on geometrical parameters, inductance is estimated using either positive slope or negative slope, whichever has higher number of current samples. This ensures that there are always enough samples to obtain an estimation within desired error bounds.

Lastly, current samples are categorized into rising or falling at real time. Instead of using a voltage sensor, the algorithm makes use of the fact that the successive switching period's duty ratio is known once the control law is executed. The successive α is calculated by (4.9), where V_{avg} is the output of the control law.

$$\alpha = \frac{V_{av}}{2V_{dc}} + 0.5 \tag{4.9}$$

The firing instants of gate signals $T1, T2, T3, T4$ in Fig. 4.1 are decided for the successive period. A counter t_{count} emulates the time steps of the switching period. By this, the digital computer is at all times aware of the output voltage sign (V_{dc} or $-V_{dc}$) and hence the slope direction, and accordingly stores the current samples in corresponding category ($\mathbf{i}^+$ or $\mathbf{i}^-$). Systematic flow of the algorithm is given in Fig. 4.3.

4.1.2 Resistance Estimation

The single slope detection is susceptible to resistance change. The estimated value from positive and negative slope is equal only if the resistance is accurately known. In practical systems, the resistance changes due to temperature drifts. Therefore, for proper working of single slope detection algorithm, accurate resistance value is required. In this section, resistance estimation is proposed by using both positive and negative slopes within one switching period. But since the time constant for resistance change due to temperature is much larger than the EML time constant, a deliberate cycle of fixed duty ratio ($0.45 \sim 0.55$) to allow for sufficient time (samples) for rising and falling interval (double slope cycle) is injected at intermittent instants with time period T_R as shown in Fig. 4.4. The EML control and air gap estimation proceeds unaffected and the available DC voltage also does not decrease.

Equating (4.6) and (4.8), and with some algebraic manipulation estimated resistance is expressed as:

$$R_{est} = \frac{V_{dc}(\frac{\Delta i^-}{\Delta t} + \frac{\Delta i^+}{\Delta t})}{\bar{i}^+ \frac{\Delta i^-}{\Delta t} - \bar{i}^- \frac{\Delta i^+}{\Delta t}} \tag{4.10}$$

Where R is replaced by R_{est}. It is observed, later in experiments, that resistance update after every T_R causes sudden changes in air gap estimation. This is associated to the fact that inductance changes suddenly once resistance updates, causing a sudden change in detected air gap due to its low sensitivity. To compensate it, estimated resistance is passed through a simple first order low pass filter with a high time constant τ_R. This smooths the detected resistance value. In addition, (4.10) is invalid for cases when the denominator is zero. Physically, it is equivalent to saying $i_{avg} = 0$, where i_{avg} is the average current of one switching period. Practically, it has no fatal effects since, when $i_{avg} = 0$, the effect of the term $\bar{i}^+R$ in (4.6) is minimal. This is avoided by a coding routine which uses nominal R at $i_{avg} = 0$.

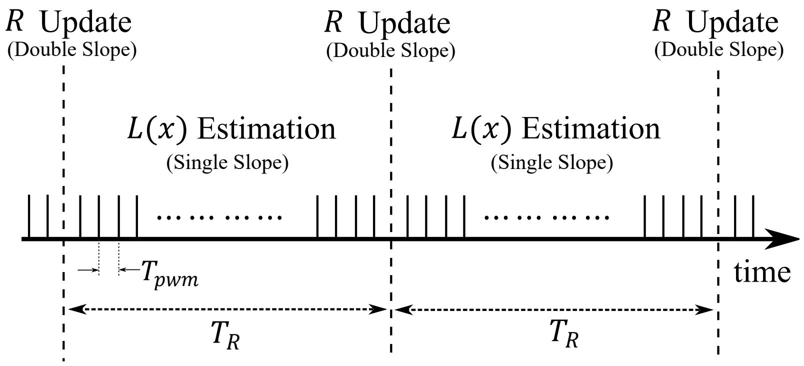

Figure 4.4: Resistance detection by intermittent double slope cycles with time period T_R

4.1.3 Numerical Case Study: Single Slope Detection Method

The proposed algorithm is verified first by a numerical case study. Matlab/Simulink is used for simulations. EML plant is modeled in Simulink by (2.1) and (4.2). The experimentally obtained relation between $L(x)$ and $x(t)$ is used, and consequently $\frac{\partial L(x)}{\partial x}$ for f_{mag} model, thus all un-modeled dynamics such as leakage flux, fringing etc in the magnetic circuit are accounted for. Table 4.1 shows the parameter values used in numerical case study as well as experiment. Two feedback control loops are employed. Outer loop constitutes the Proportional-Derivative (PD) control law, used to stabilize air gap. Inner Proportional-Integral (PI) control law is used to control coil current. The controller gains are obtained by polynomial design approach using Manabe's Canonical form solved for the respective plant's transfer functions as shown in Chapter 3. Finally the estimation algorithm is implemented in S-function block of Simulink. The schematic of the feedback loop and the proposed estimated algorithm is shown Fig. 4.5.

The plant is stabilized at nominal point (i_0, x_0). Simulation results for the proposed algorithm are shown in Fig. 4.6 with clean and a noisy current signal. In both cases, the estimated signal stabilizes the plant. However, it is observed that x_{est} estimation error is strongly susceptible to current measurement noise. Furthermore, a resistance change by $0.1[\Omega]$ causes the L^+_{est} and L^-_{est} to drift apart, consequently, detected signals also change. This is as shown in Fig. 4.7. Therefore, resistance estimation is essential for single slope detection method.

4.1.4 Experimental Verification: Single Slope Detection Method

Experimental verification of the proposed method is carried on an indigenously built test bench in our laboratory. Since accurate current information is vital for good estimation, it is important to employ a good current sensor with sufficient sensitivity to detect current-ripple and adequate bandwidth. Also, in design of the current sensor PCB, care should be

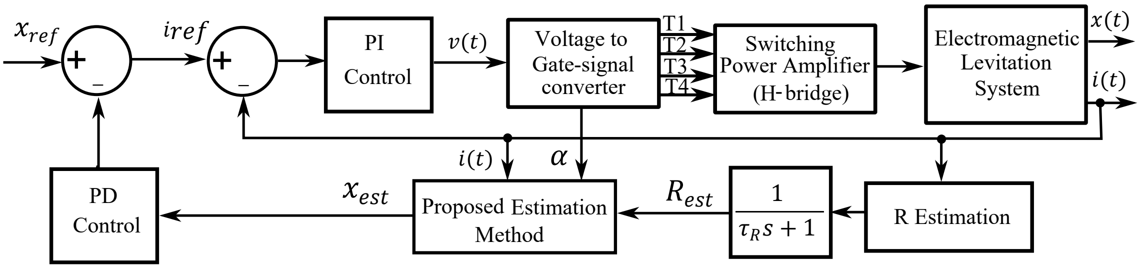

Figure 4.5: Schematic of the feedback control loop and proposed estimation method.

Table 4.1: Numerical values used in simulations/experiments

Parameters	**Value**
m [kg]	0.965
N	400
V_{dc} [V]	45
T_{pwm} [sec]	2×10^{-3}
T_s [sec]	1.25×10^{-6}
T_R [sec]	0.4
τ_R [sec]	5
R [Ω]	1.7
x_0 [m]	8×10^{-3}
i_0 [A]	4.04
L_0 [H]	24.1×10^{-3}

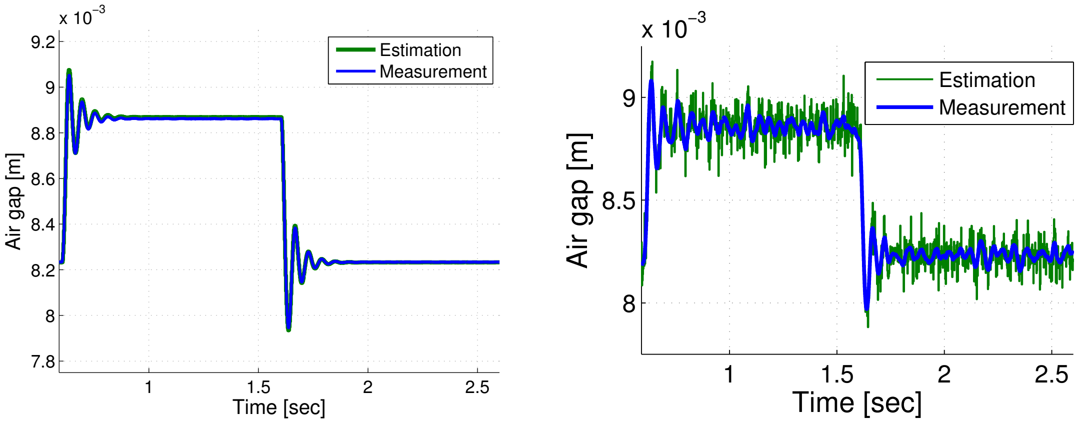

(a) (b)

Figure 4.6: Simulation results of air gap estimation with and without current noise: (a) With clean current signal. (b) With noisy(σ^2=10^{-3}) current signal.

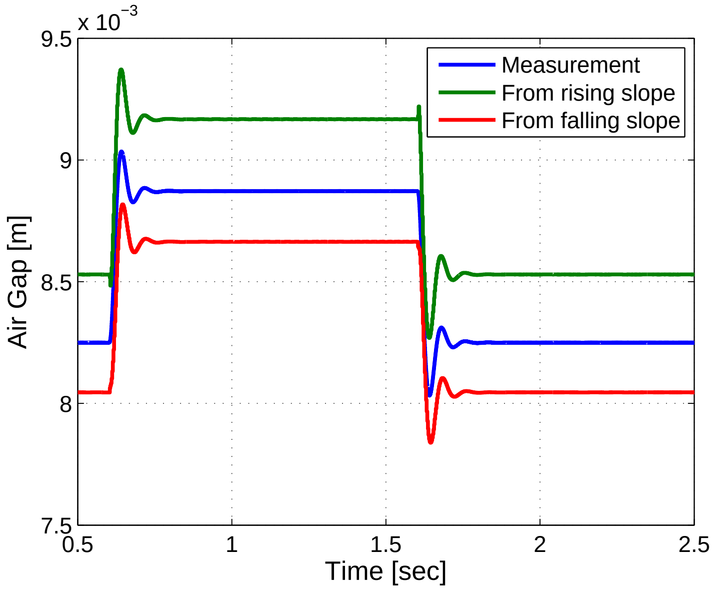

Figure 4.7: Effect of resistance shift due to temperature change on detected air gap signals.

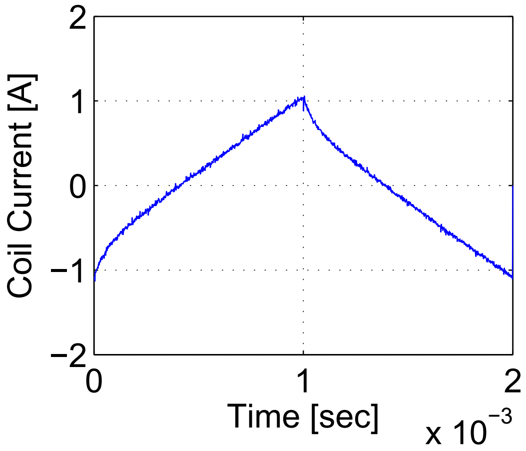

Figure 4.8: Measured current-ripple for 1 T_{pwm}

taken to reduce measurement noise. The current sensor used in our experiment is LEM LTSR 6-NP with a sensitivity of 206 [mV/A]. Air gap sensor, Omron Z4W-V25R LED Displacement Sensor, is only used to log measured air gap for comparison purposes.

Figure 4.8 shows the measured current ripple for one switching period. The noise in the measurement causes the slope estimation to have large variance which does not produce air gap signal within acceptable error bounds. Furthermore, rail core used for translation motion vehicle has significant amount of eddy currents. In our system alike, the instants right after switching are influenced greatly by the eddy currents, dying out after approx $150[\mu\text{sec}]$. Thus, rendering those instants useless in slope calculation. Remaining current-ripple region produces accurate slope estimation only if noise is small enough or there are sufficiently large number of current samples.

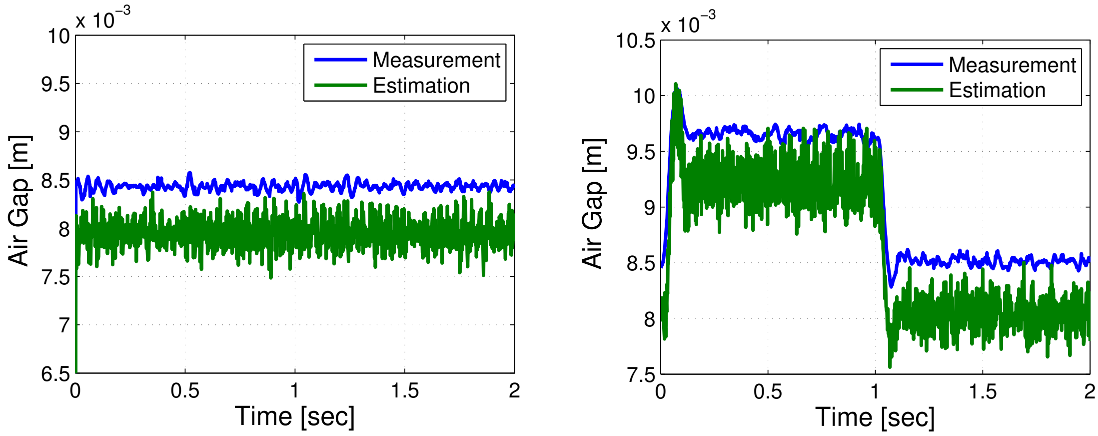

(a) (b)

,

Figure 4.9: Stable levitation with x_{est} as feedback: (a) Stable levitation. (b) Step response.

In experiment, the noise from current sensor, though not obviously visible, causes poor estimation and therefore to allow for good estimation, a switching period T_{pwm} of 2×10^{-3}[sec] is used. With ADC sampling time $T_s = 1.25 \times 10^{-6}$[sec], it allows 1600 samples in one period with minimum samples of 800 for each slope calculation. This choice for T_{pwm} and T_s produces acceptable error for stable levitation.

Using the controller gains from numerical case study (with slight tuning), the results are shown in Fig. 4.9. Figure 4.9(a) shows that at stand still, the levitating object is stabilized at the nominal gap length. Though vibrations of amplitude 0.1[mm] are observed. These will be dealt in the next section. A small offset in the estimated and measured signal is present. Since around 8[mm], the sensitivity is low, therefore a small mismatch between actual value and the experimental curve $x_{est} = f(L(x))$ results in an offset error. The aim is to achieve stable levitation and not reference tracking, thus we choose to ignore this offset.

Experimental verification of resistance detection algorithm is shown in Fig. 4.10. By levitating at 9.5[mm], increased current causes temperature rise and consequently resistance change. Fig. 4.10(a) shows the estimated resistance. With a change of $0.3[\Omega]$, x_{est}, without R compensation, drifts down to 8[mm] from 9.3[mm] as shown in Fig. 4.10(b). On the contrary, by using the proposed R detection algorithm, x_{est} remains around the nominal value demonstrating the practical goodness of this method.

4.1.5 Statistical analysis of current-ripple: Deciding switching time period T_{pwm}

An important parameter in the proposed sensorless method is the switching period T_{pwm}. It affects the applied control performance as well as estimated air gap quality in terms

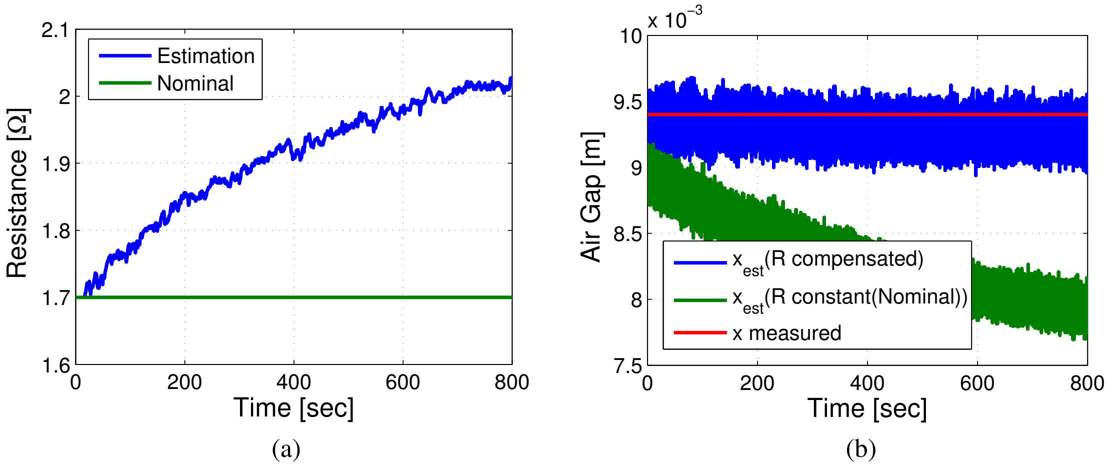

Figure 4.10: Resistance estimation algorithm: (a) Estimated resistance. (b) Comparision of air gap estimation with and without R compensation.

of noise variance. Therefore, care should be taken while setting such a vital parameter. A statistical analysis is carried out to determine an acceptable switching period which provides sufficiently fast actuation for stabilization as well as enough time interval for current sampling to estimate air gap. Levitating carrier is mechanical fixed at a known gap length of 8 [mm]. Coil is exited by a switching voltage of $\alpha = 0.5$. The resulting coil current is sampled at $T_s = 1.25 \times 10^{-6}$[sec] and 1000 switching periods are logged. This step is repeated for three switching periods $T_{pwm} = 1, 1.5, 2$[ms]. All 1000 periods for each case are represented overlapped in Fig. 4.11. The presence of noise in current measurement is observed in each case. Furthermore, the instants right after switching are unusable since they are influenced by eddy currents [26]. Therefore, those current samples are dropped out of slope calculation. The ratio of length of usable interval to the noise width for $T_{pwm} = 1$[ms] is minimum. Higher this ratio, lower is the variance of calculated slope. This is illustrated by plotting the calculated slope for each of 1000 periods as a distribution expressed in Fig. 4.12. Since the noise in current measurement

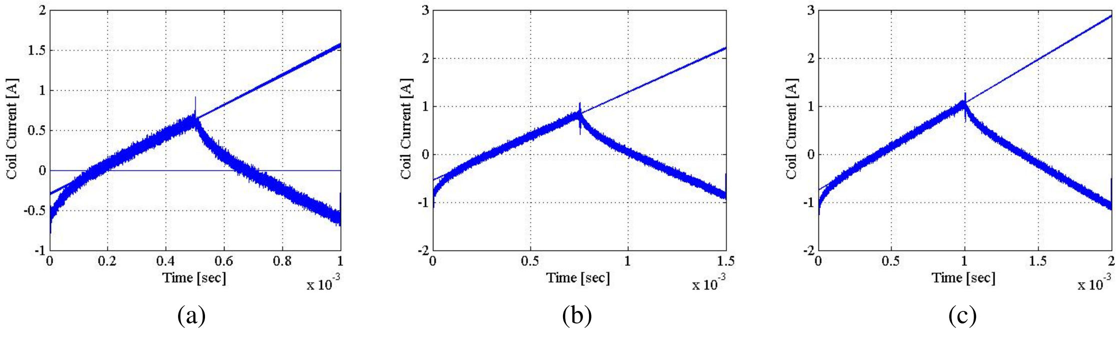

Figure 4.11: Current-ripple and its straight line approximation for 1000 switching periods T_{pwm} overlapped: (a) 1[ms] (b) 1.5[ms] (c) 2[ms]

Table 4.2: Results for statistical analysis of current-ripple at different switching periods

T_{pwm}[ms]	1	1.5	2
$slope_{avg}$[A/s]	1861	1832	1813
σ_{slope}[A/s]	10.4268	5.0670	3.2584
x_{avg}[m]	0.0083	0.0079	0.0076
σ_x [m]	1.3993×10^{-04}	4.7512×10^{-05}	3.9861×10^{-05}

is white, an approximate normal distribution is expected. Proceeding forward with single slope detection algorithm, the air gap distribution for the three cases is also illustrated in Fig. 4.13 with third case ($T_{pwm} = 2$[ms]) having least variance σ_x^2 and being the most suitable out of the three for low noise sensorless gap estimation. Respective mean values and standard deviation σ of slope and air gap are calculated and shown in table 4.2.

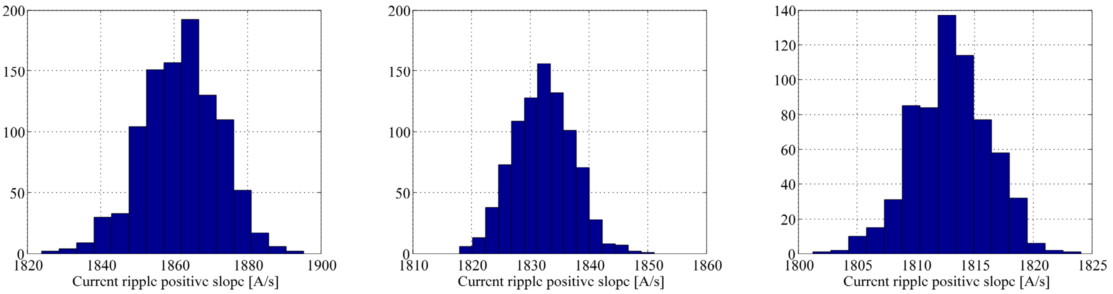

(a) (b) (c)

Figure 4.12: Statistical distribution of slope calculation for 1000 switching periods T_{pwm}: (a) 1[ms] (b) 1.5[ms] (c) 2[ms]

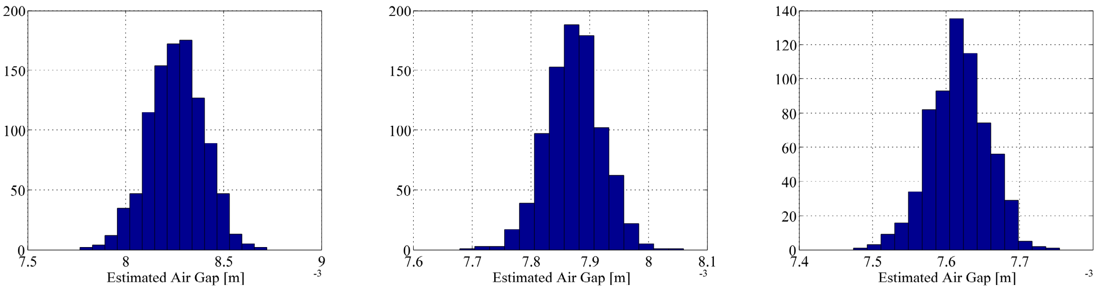

(a) (b) (c)

Figure 4.13: Statistical distribution of estimated air gap for 1000 switching periods T_{pwm}: (a) 1[ms] (b) 1.5[ms] (c) 2[ms]

For the same mechanical air gap, the average gap length is observed to be different in each case. This is attributed to the fact that the actual ripple is not linear, but rather an exponential curve with decreasing slope and for large T_{pwm} this fact cannot be ignored.

It is also evident in the table 4.2 with slight decrease in slopes from $T_{pwm} = 1$[ms] to $T_{pwm} = 2$[ms]. Further increase in T_{pwm} to obtain better estimation performance is fatal since it will limit allowable dynamic frequency range for control. Other ways to achieve this is of course to decrease the current sampling T_s which in our current hardware setup is not possible and may be considered in future.

4.1.6 Weighted Current-Ripple Slopes Detection Method

It is observed that the single slope detection method works well, however, during transients when the duty ratio changes from $\alpha < 0.5$ to $\alpha > 0.5$, the input data for inductance estimation changes from falling current-ripple to rising one. As a result, the detected air gap signal has a discontinuity at that instant. Since later in Chapter 5, zero power control is applied to the EML system, which forces the duty ratio to around 0.5, it is relevant to deal with this discontinuity here. Furthermore, in situations when duty ratio is around 0.5, as in zero power, it is natural and optimal case to extract air gap information from both rising and falling current-ripples. But such double slope detection methods ([25],[23]) cannot be applied for duty ratio variation to extremes $(0.2$ or $0.8)$. In such cases, the detection should shift to single slope detection which provides a better dynamic accuracy.

With respect to the above discussion, we have proposed a method to use single slope as well as double slope information in air gap estimation. However, their respective operating regions are decided based on weights which are functions of duty ratio α.

Under this approach, the estimated inductance L_{est} is expressed as follows:

$$L_{est} = w_1(\alpha)L_{est}^{+} + w_2(\alpha)L_{est}^{-} \tag{4.11}$$

Where w_1 and w_2 are respective weight functions of duty ratio. The weights have a constraint that their sum never exceeds one:

$$w_1(\alpha) + w_2(\alpha) = 1 \tag{4.12}$$

This allows for analyzing and choosing just a single weight. Figure 4.14 shows different types of functions that can be used as weights. Figure. 4.14(a) represents the behavior of previous single slope detection method presented in section 4.1.1. Figure. 4.14(b) shows the sigmoid function that translates the duty ratio input to weights. This function represents good mathematical properties, but for extreme values of duty ratio, one weight approaches 1 and other reaches 0, but neither are exactly 1 or 0. This causes slight interference from low accuracy slope information to the better one, resulting in dynamic noise in the detected air gap signal.

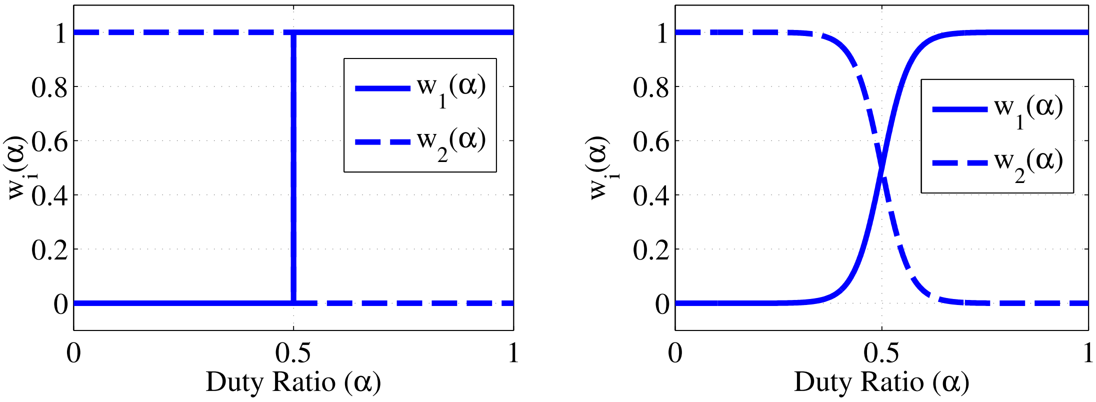

(a) (b)

,

Figure 4.14: Types of allowable weight functions: (a) Step like function used for single slope method. (b) Sigmoid function.

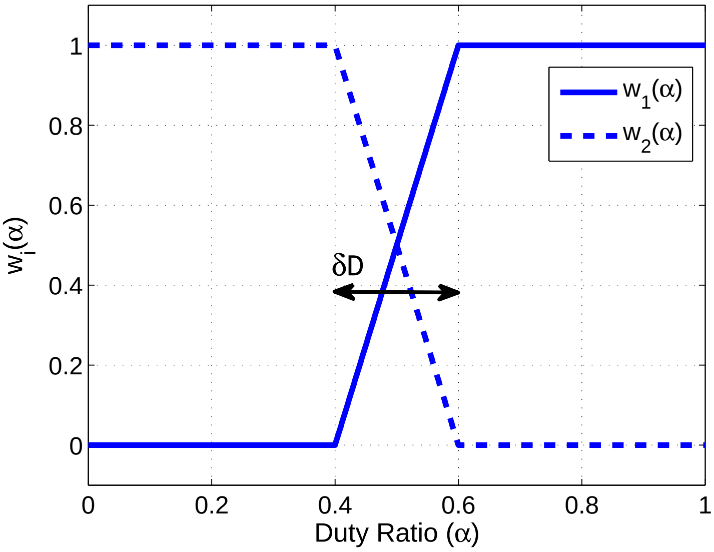

Figure 4.15: Piece wise linear weight function

It is better to reject the noisy slope information explicitly. That is done by employing the piece wise linear function shown in Fig. 4.15 and given as:

$$w_1(\alpha) = \begin{cases} 0 & 0 \le \alpha < (0.5 - \frac{\delta D}{2}) \\ \frac{1}{\delta D}(\alpha - 0.5) + 0.5 & (0.5 - \frac{\delta D}{2}) \le \alpha \le (0.5 + \frac{\delta D}{2}) \\ 1 & (0.5 + \frac{\delta D}{2}) < \alpha \le 1 \end{cases} \tag{4.13}$$

Where δD is the width of linear range. This maintains a linear contribution from both slopes till either one has samples below a pre-determined threshold. After which only one slope information is used. Furthermore, from hardware's perspective, it is also lighter and faster in implementation compared to complex functions such as sigmoid function.

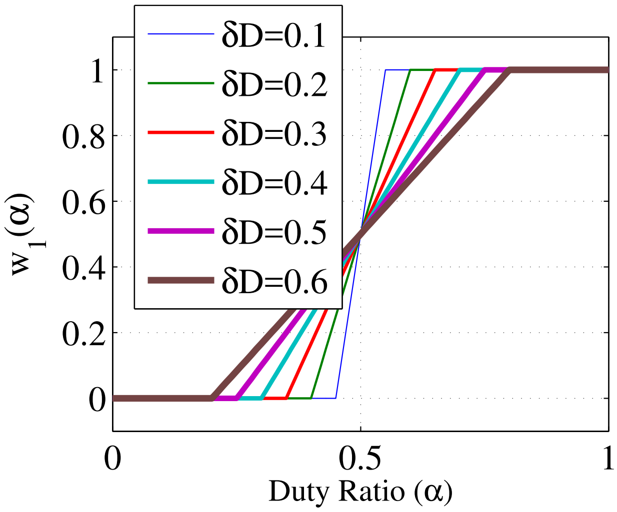

Figure 4.16: Possible shapes of Piece wise weight function ($0.1 < \Delta D < 0.6$)

Figure 4.16 shows piece wise weight functions with varying linear range δD. Choice of δD depends on a statistical analysis of double slope and single slope methods and choosing an appropriate range based on least dynamic error.

4.1.7 Statistical Comparison between Double Slope, Single Slope and Weighted Slopes Methods

Statistical advantage of the prosed weighted slopes method over double slope and single slope method is experimentally verified by comparing the quality of estimated inductance L_{est} in each case. Position of levitated object is fixed at about 8[mm] which corresponds to $L(x) = 24.1 \times 10^{-3}$[H]. Electromagnetic coil is excited with simultaneous execution of double , single and weighted slopes detection methods, outputs of which are L^{*}_{est},L^{+}_{est},L_{est} respectively. The duty ratio α is varied from 0.5 to 0.82 and estimated inductances are logged. At each value of α, inductance is calculated 1000 times. This allows calculation of noise spread at each value of α.

Since with $V_{dc} = 45$[V] and $\alpha = 0.82$, the steady state current exceeds the maximum allowable coil current, therefore for this analysis $V_{dc} = 15$[V]. The consequence of such change results in increased estimation noise. But since it is a comparison analysis, all three cases are equally affected. The spread of normalized estimated inductance is shown in Fig. 4.17. It is evident from Fig. 4.17(b) that double slope method has least noise around $\alpha = 0.5$. But it increases exponentially as α approaches its extreme value. This is due to the decrease in number of current-ripple samples for the falling interval. The single slope method shows robustness towards α change. However, its noise spread is larger than double slope method for α near 0.5. Secondly, single slope is also susceptible

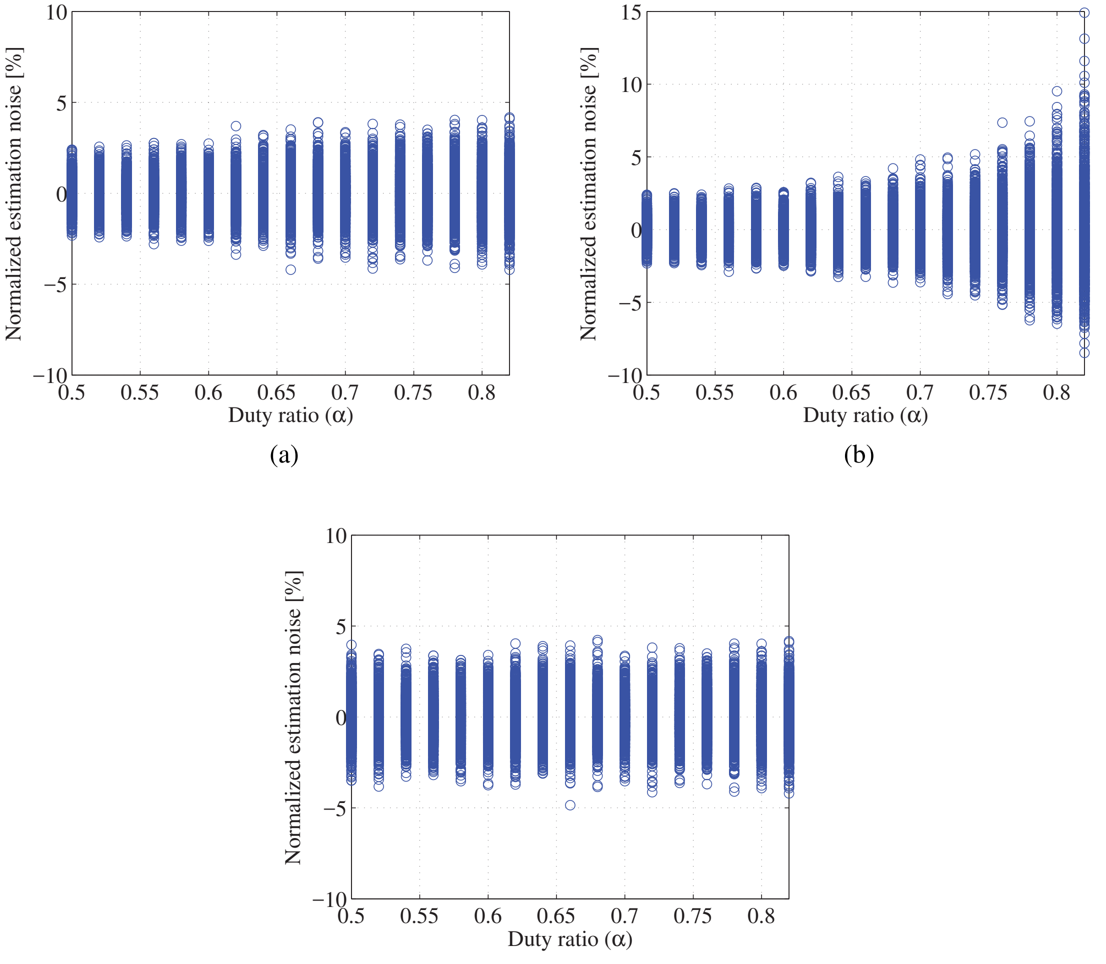

(a) (b) (c)

Figure 4.17: Normalized estimated inductance noise: (a) Weighted slopes method. (b) Double slope method. (c) Single slope method.

to resistance change which we have not considered in this analysis. Weighted slopes method combines the advantages of both as shown in Fig. 4.17(a). Weights depending on α are calculated using the piece-wise function (Fig. 4.16) which exploits the low noise characteristic of double slope method at $\alpha \approx 0.5$ and robustness of single slope method for large values of α. The above information can be represented in a more compact form by calculating the standard deviation σ for each case as shown in Fig. 4.18. The piece wise function's paramter δD is set by choosing the value of α where L^{*}_{est} and L^{+}_{est}'s trend intersect each other which in this case is 0.7 resulting in $\delta D = 0.4$.

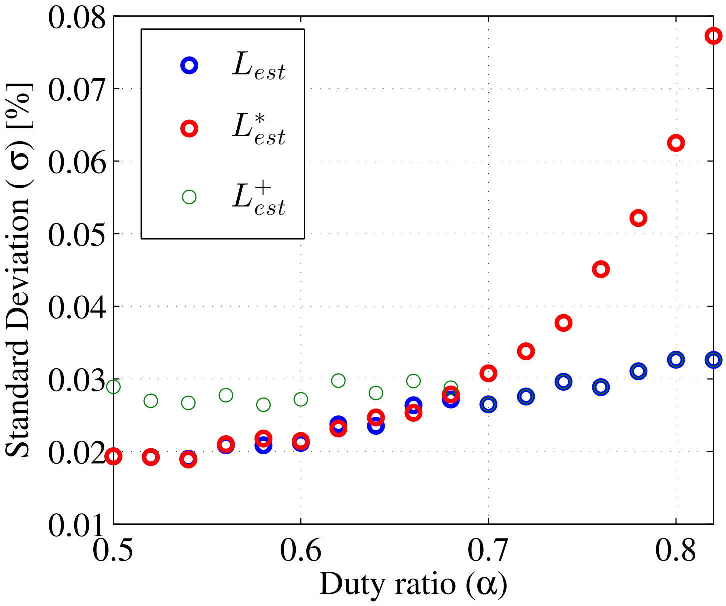

Figure 4.18: Standard deviation σ of normalized estimated inductance noise

4.2 Noise Suppression Strategy for Sensorless Air Gap Detection Algorithm using State Observer

Output of the proposed air gap detector as previously shown in experimental results (Fig. 4.9) has considerable noise. Although, it is sufficient to achieve stabilization, but quality of the control response is not acceptable. The levitating carrier displays minute oscillations about its operating point.

This noise, in fact, originates from current signal and propagates all the way to detected air gap signal. The noise can be reduced by using a high quality data acquisition hardware as well as a good current sensor. In our experimental test bench, the ADC input range is only 3[V] and current sensor measuring range is from -2[A] to 9[A] with a sensitivity of 206[mV/A]. That means , for example, a current change of 50[mA] produces 10.8[mV] which in our case is in the range of electrical noise. By using better hardware, the Signal to Noise Ratio (SNR) of current signal can be improved and ,consequently, the detected air gap signal as well. But in case when changes in hardware is not possible, signal processing techniques much be employed for the said purpose.

Furthermore, since velocity signal adds artificial damping for EML systems, its signal quality must be good. Noise in the air gap signal puts an upper limit on the proportional gain and in velocity signal it adds an upper limit to the value of derivative gain. Even, if hardware can provide high power for an improved control performance, because of noise the available hardware potential cannot be fully tapped. Therefore, in order to achieve

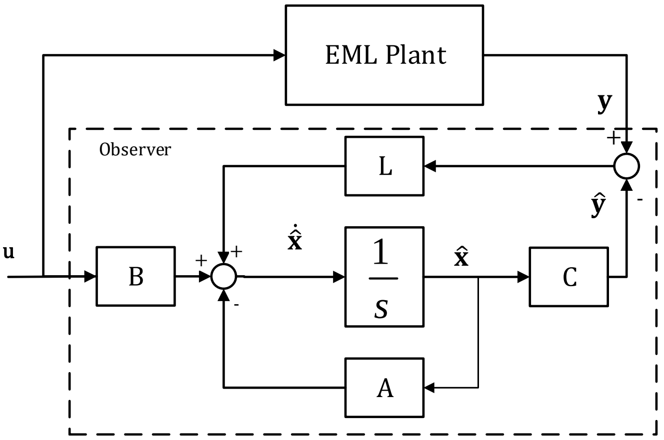

Figure 4.19: Schematic of a state observer.

an acceptable signal for air gap and velocity, we propose to treat the air gap detection algorithm as a noisy sensor, and combine it with a state observer. This outputs conditioned signals with high Signal to Noise Ratio (SNR).

4.2.1 State Observer Design

For a dynamical system represented by a standard state space model as shown in (4.14) , a schematic of the state observer is shown in Fig. 4.19.

$$\begin{aligned}\dot{\mathbf{x}} &= \mathbf{A}\mathbf{x} + \mathbf{B}\mathbf{u} \\ \mathbf{y} &= \mathbf{C}\mathbf{x}\end{aligned} \tag{4.14}$$

The state observer's (Luenberger observer) dynamic equation is given as:

$$\dot{\hat{\mathbf{x}}} = \mathbf{A}\hat{\mathbf{x}} + \mathbf{B}\mathbf{u} + \mathbf{L}(\mathbf{y} - \mathbf{C}\hat{\mathbf{x}}) \tag{4.15}$$

$$\dot{\hat{\mathbf{x}}} = (\mathbf{A} - \mathbf{L}\mathbf{C})\hat{\mathbf{x}} + \mathbf{B}\mathbf{u} + \mathbf{L}\mathbf{y} \tag{4.16}$$

Where $\hat{\mathbf{x}}$ is the estimated state vector and $\mathbf{L}$ is the observer gain vector. The design procedure involves choosing appropriate gains so that observer system converges to the actual plant states. For the second order system define by 2.21, the observer equation is written as:

$$\begin{bmatrix}\Delta\dot{\hat{x}}(t)\\ \Delta\ddot{\hat{x}}(t)\end{bmatrix} = \left(\begin{bmatrix}0 & 1\\ -\frac{k_x}{m} & 0\end{bmatrix} - \begin{bmatrix}l_1\\ l_2\end{bmatrix}\begin{bmatrix}1 & 0\end{bmatrix}\right)\begin{bmatrix}\Delta\hat{x}(t)\\ \Delta\dot{\hat{x}}(t)\end{bmatrix} + \begin{bmatrix}0\\ -\frac{k_i}{m}\end{bmatrix}\Delta i(t) + \begin{bmatrix}l_1\\ l_2\end{bmatrix} y(t) \tag{4.17}$$

In order to calculate observer gains, characteristic equation for the above system is derived and equated to a desired polynomial as shown below:

$$|s\mathbf{I} - (\mathbf{A} - \mathbf{LC})| = s^2 + l_1 s + \frac{k_x}{m} + l_2 \tag{4.18}$$

Equating it to a desired polynomial $1 + \tau_0 s + \frac{\tau_0^2}{2.5} s^2 = 0$ which is calculated by using the

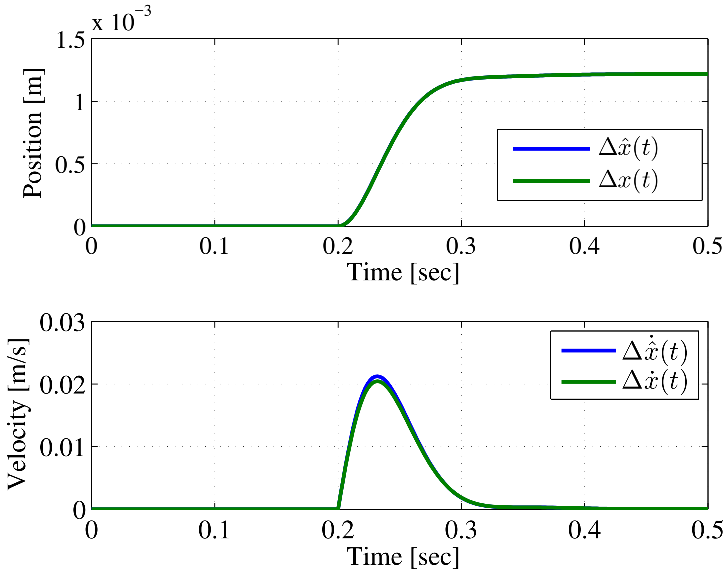

Figure 4.20: Observer results for nominal plant

Manabe's coefficient method as was shown in Chapter 3, the gains are calculated. τ_O is the tuning parameter with which the speed of convergence for the observer is controlled. Since the our sensorless estimation signal is noisy, a high τ_O would be better so that noise can be smoothed out. But care must be taken so as to not let it exceed to the point that it disrupts controller performance. For controller with $\tau = 0.05$, we choose $\tau_O = 0.01$. The simulation results for nominal plant are shown in Fig. 4.20. But this is an ideal case, in reality there are bound to be differences between nominal plant and real plant. The effect of such differences can be observed when the same observer is simulated with non linear plant as shown in Fig. 4.21. A fatal effect is seen in the estimation of velocity term, which does not converge to zero. An offset is always present. This offset is related to the nonlinearity and unmodelled dynamics at positions other than nominal one. Since velocity is not zero, a stable feedback system cannot be established. There are different methods to deal with this problem. We deal with it by using a disturbance observer [30].

4.2.2 Disturbance Observer Design

A conceptual diagram for a disturbance observer (DOB) is shown in Fig. 4.22, where $G_p(s)$ is the actual plant, G_{po} is the nominal plant, $Q(s)$ is a low pass filter, $d(s)$ is a

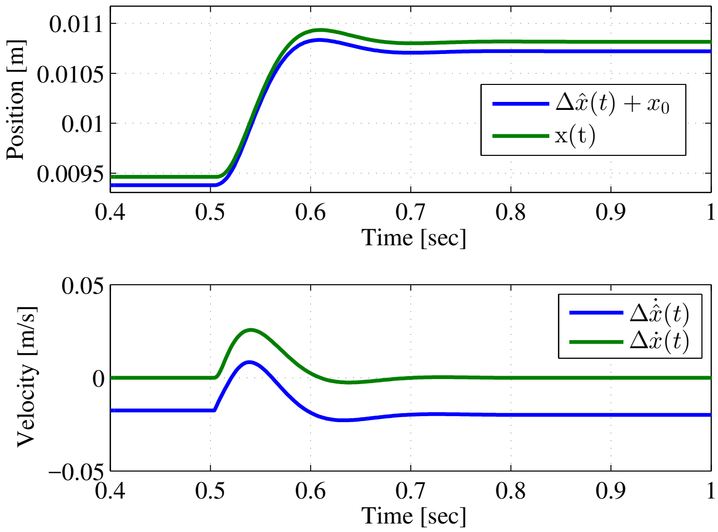

Figure 4.21: Obsever results for non linear plant.

disturbance, $N(s)$ is the sensor noise and $\hat{d}(s)$ is the estimated disturbance. The relation between inputs $I(s), d(s), N(s)$ to output $X(s)$ is given as:

$$X(s) = \frac{G_p G_{po}}{G_{po} + Q(G_p - G_{po})} I(s) + \frac{(1-Q) G_p G_{po}}{G_{po} + Q(G_p - G_{po})} d(s) + \frac{Q G_p}{G_{po} + Q(G_p - G_{po})} N(s) \tag{4.19}$$

For $Q(s) = 1$, $X(s) = G_{po} I(s) + N(s)$ meaning that the differences between real and nominal plant, which are taken as lumped disturbance are compensated. This feature of DOB is called nominal plant following. However, for cases when G_{po}^{-1} is non-causal system, implementation is impossible. Therefore, a slight alteration is done in the block diagram as shown in Fig. 4.23 such that the relative degree (difference between the order of denominator and numerator) of term $Q(s)G_{po}^{-1}$ is zero or positive rendering it realizable.

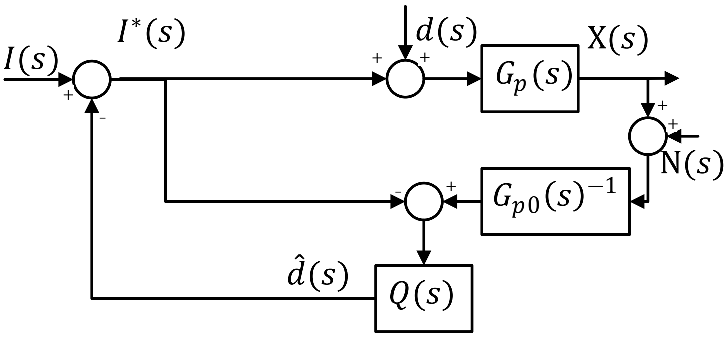

Figure 4.22: Disturbance observer conceptual diagram.

$Q(s)$ is usually designed as a low pass filter. This is because the external disturbance and parameter uncertainty, practically lie in the low frequency region. Furthermore, by proper adjustment of cut off frequency of $Q(s)$, sensor noise is attenuated. Since, EML nominal plant given in (2.15) is second order, the $Q(s)$ filter's form taken in our simulation is given as:

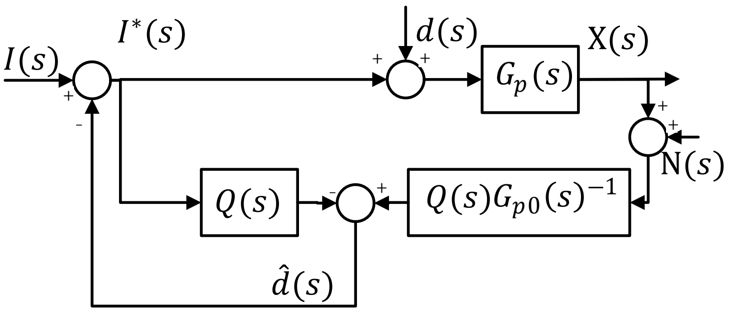

Figure 4.23: Disturbance observer for compensating uncausal inverse system.

$$Q(s) = \frac{1}{\frac{\tau_Q^2}{2.5}s^2 + \tau_Q s + 1} \tag{4.20}$$

Here, τ_Q is the time coefficient used to adjust filter's cut off frequency. In designing the state observer and DOB, only τ_O and τ_Q are tuned to achieve desired performance. But these have a limited range. The upper limit is restricted by τ (tuning parameter for air gap controller) so as to not cause sufficiently large delays and compromise stability. The allowable range for τ_0 is given as:

$$\tau_0 < 0.2\tau{\sim}0.4\tau \tag{4.21}$$

The choice of τ_Q effects the speed of disturbance estimation. Since nominal plant following involves estimating the nonlinearity and adding a constant feed forward bias to compensate it, its speed should be faster than the air gap controller. Thus similar constraints as in (4.21) are valid for τ_Q too. Selecting $\tau_Q = 0.01$ and $\tau_O = 0.01$, observer gains are calculated and a simulation is carried out to test the working of state observer estimation with DOB nominal plant following. The result for a step command at 0.5[sec] is shown in Fig. 4.24. Comparing this with the previous simulation (Fig. 4.21), due to the disturbance compensation, the state observer estimates the actual air gap and velocity with no offset. In both cases, the controller parameters used are same. However, due to the difference between actual and nominal plant, the step response in Fig. 4.21 is not the designed one. Since with DOB, the actual plant follows nominal plant, along with correctness of state estimation, the designed control action is also achieved. This is inferred by comparing it .Fig. 4.20. Furthermore, it should be noted that though there is no

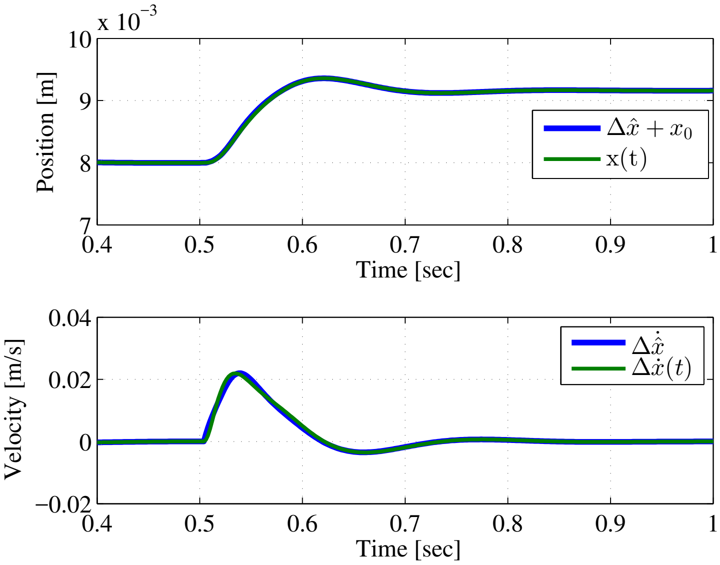

Figure 4.24: State obsever output with DOB nominal plant following

external disturbance but the DOB still outputs a value as shown in Fig. 4.25. This output represents the parameter uncertainty of the actual plant from the nominal values. A step command moves the levitating object by 1[mm] resulting in change in plant parameters which is then estimated by the DOB.

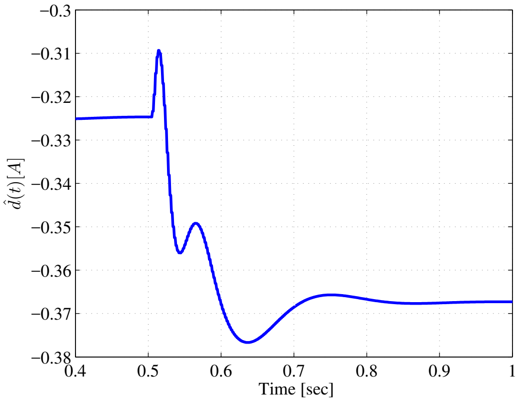

Figure 4.25: Plant parameter uncertainty/non-linearity as lumped estimated disturbance.

4.2.3 Numerical Case Study

A numerical case study is conducted for verifying the noise suppression strategy as shown in Fig. 4.26 in Matlab/Simulink. The parameters used are given in Table 4.3. The air gap

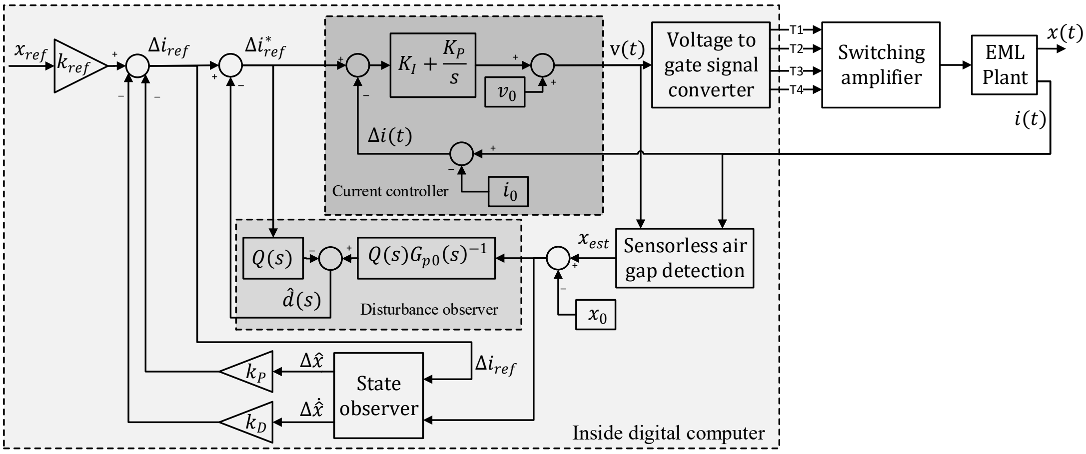

Figure 4.26: Noise suppression strategy by state observer.

Table 4.3: Parameter values for numerical case study of state observer with dob plant following

Parameters	**Value**	**Parameters**	**Value**
m [kg]	1.165	T_s[sec]	1.25×10^{-6}
V_{dc} [V]	45	T_{pwm} [sec]	2×10^{-3}
R [Ω]	1.7	x_0 [m]	8×10^{-3}
i_0 [A]	4.4	L_0 [H]	24.1×10^{-3}
k_i [N/A]	4.50	k_x [N/m]	-2.24×10^3
τ [sec]	0.05	τ_c[sec]	0.01
k_P [A/m]	-756	k_D[As/m]	-10.34
K_P [V/A]	4.33	K_I[V/As]	6.037
τ_Q[sec]	0.01	τ_0[sec]	0.012
δD	0.4		

and current controller are designed as shown in Chapter 3. The parameters for response time of respective controllers are τ and τ_c. The inner current loop time constant τ_c is kept 10%∼30% of the outer air gap loop time constant τ.

Simulation results are shown in Fig. 4.27. For case when the current has no noise, the estimated air gap x_{est} and observer output $\Delta\hat{x}$ accurately follow the measured signal. But as noise variance in current signal is increased to $\sigma^2 = 10^{-3}$, noise starts to appear in x_{est}. However due to the noise suppression strategy, the observer outputs relatively less noisy signals ($\Delta\hat{x}$, $\Delta\dot{\hat{x}}$) which are used to achieve stable levitation as shown in Fig. 4.28. Figure 4.27(c) shows the estimated non-linearity during step response as a lumped disturbance which is feed forwarded to attain nominal plant following.

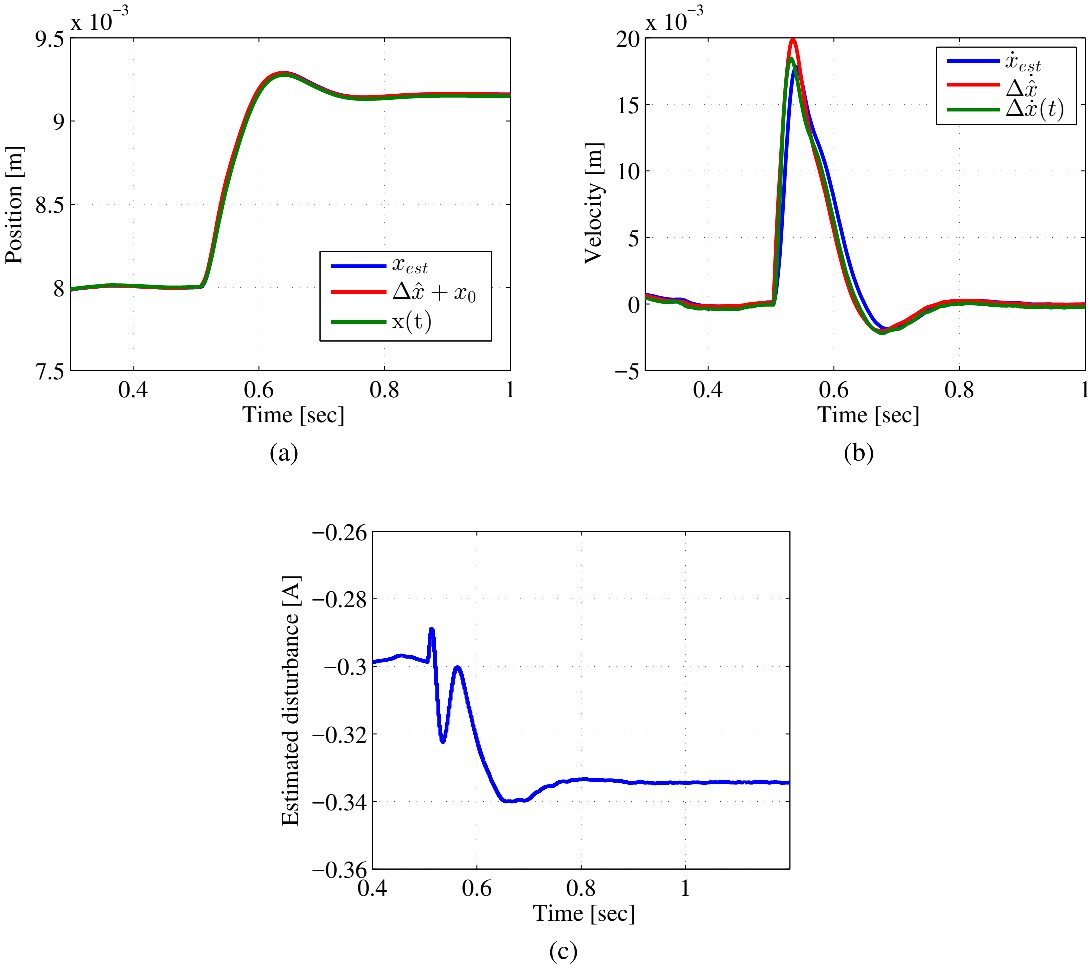

(a) (b) (c)

Figure 4.27: Simulation Results: (a) Position. (b) Velocity. (c) Estimated nonlinearity as lumped disturbance.

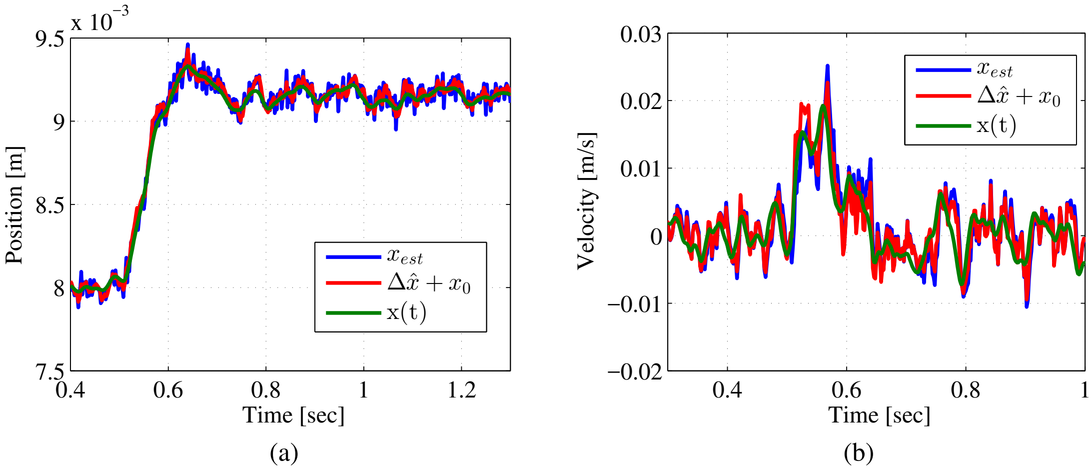

(a) (b)

Figure 4.28: Simulation Results with current noise ($\sigma^2 = 10^{-3}$): (a) Position. (b) Velocity.

4.2.4 Experimental Results

Experiments are carried out to verify the proposed strategy on the EML experimental test bench. Most of the parameters in the experiment are the same as used in numerical case study shown in Table 4.3. However, slight tuning is done for current controller and DOB (K_P=5, K_I=500, τ_Q=0.02) to obtain suitable levitation profile.

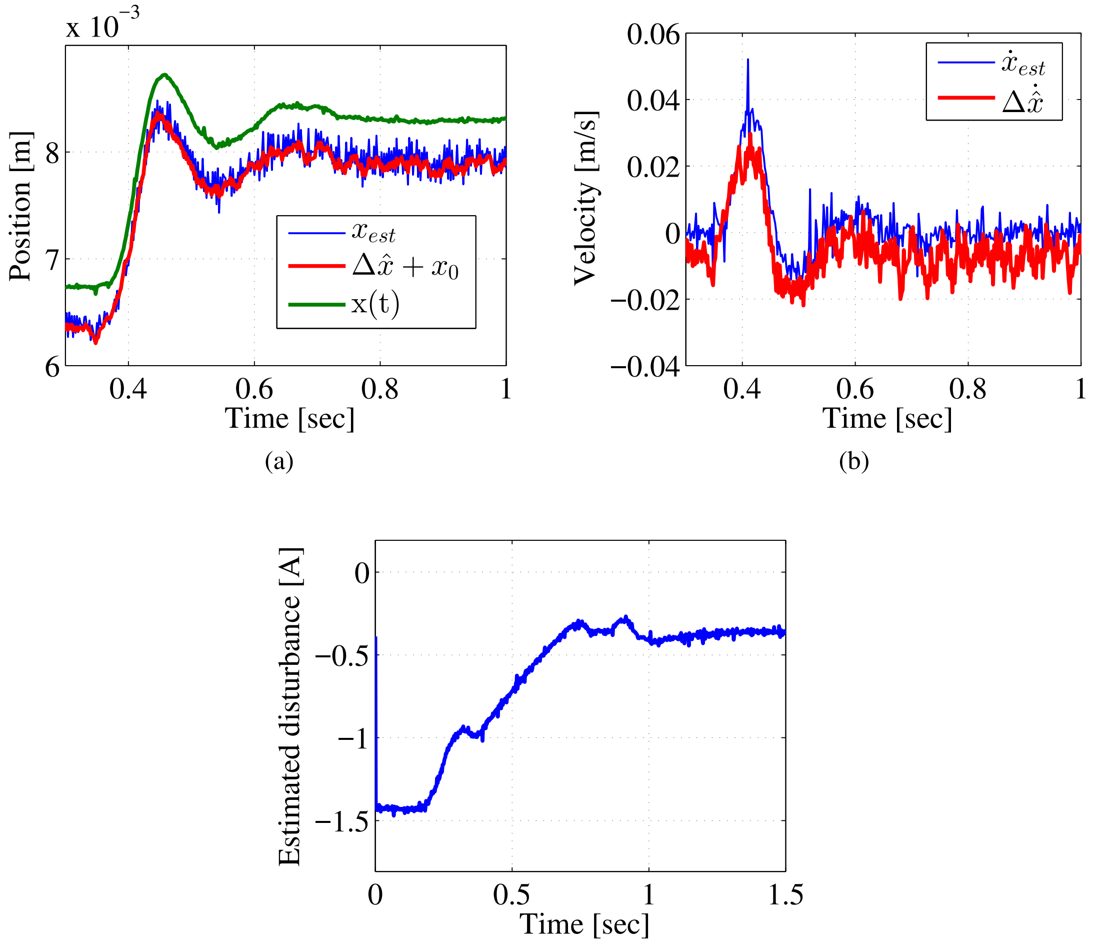

(a) (b)

(c)

Figure 4.29: Step response using air gap sensor as feedback: (a) Position. (b) Velocity. (c) Estimated nonlinearity as disturbance

At first, to verify the working of the proposed strategy, air gap signal from the sensor is used to stabilize the EML plant. Simultaneously, weighted slopes measurement method, state observer and DOB are also implemented. The position and velocity profile for a step command are shown in Fig. 4.29. The dynamic noise in the estimated air gap x_{est} and its corresponding approximate derivative $\dot{x}_{est}$ is the highest. It is noted that this estimated gap signal after being processed by the state observer gains increased SNR. The offset between measured air gap and estimated one is due to the modeling error in the inductance to air gap data base ($x_{est} = f(L)$). Since the objective is to obtain stable levitation and not position tracking, we choose to ignore this. Figure 4.29(c) shows the estimated nonlinearity when the levitated object moves from $7\sim8$[mm] as a disturbance. Finally, the schematic in Fig. 4.26 is completely implemented. The stabilization of EML plant is achieved without air gap sensor. The results are shown in Fig. 4.30. The magnified position and velocity profile is displayed to show clear improvement in the SNR of gap signal by the proposed noise suppression strategy. Furthermore, statistical analysis on the experimental results shows the decreases in standard deviation as shown below: These

Signal	**Standard deviation** σ
x_{est}	9.78×10^{-5}[m]
$\Delta\hat{x}$	5.24×10^{-5}[m]

results are promising with good prospects in industrial environment.

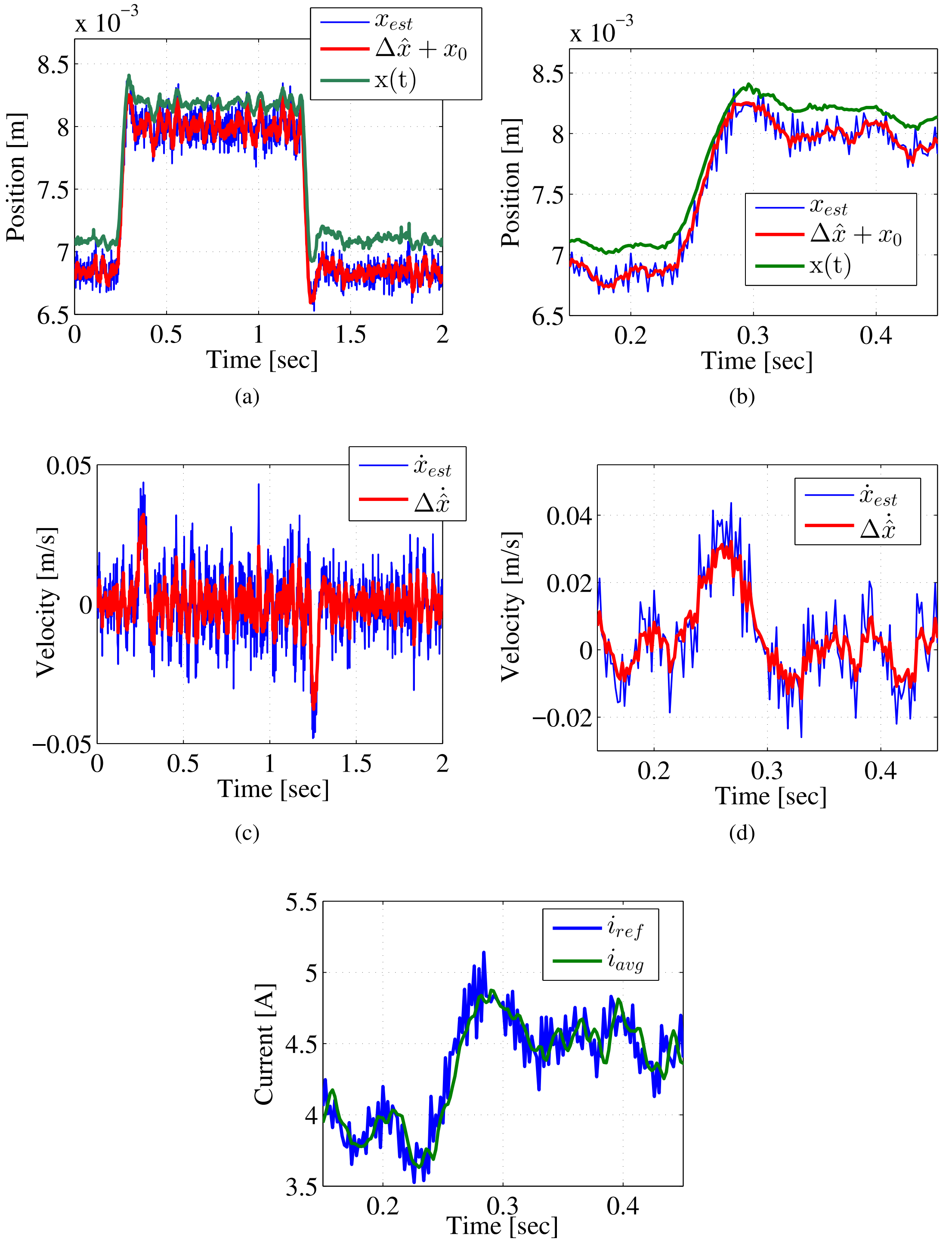

(a) (b) (c) (d) (e)

Figure 4.30: Step response using detected air gap signal as feedback: (a) Position. (b) Magnified position. (c) Velocity. (d) Magnified velocity. (e) Average current.

Chapter 5

Smart Combination of Sensorless Electromagnetic Levitation and Zero Power Control

5.1 Motivation

Of all the control methods applied for stabilization of EML systems, zero power control [9, 6, 10] stands out as the best possible control law to be combined with sensorless methods. This ensures that the average steady stage current is zero and the net weight of the levitated carrier is compensated by the force due to permanent magnet only. Zero power control not only minimizes power consumption but also enhances certain features of our proposed sensorless method. The requirement of 0.5 duty ratio for least dynamic noise is for most part fulfilled as zero power maintains a constant zero average coil current i.e both positive and negative slopes can be estimated with sufficiently large accuracy and consequently the detected air gap has low noise. Furthermore, due to slight modeling error in inductance vs air gap profile which is used to calculate air gap, an error offset is present. Zero power being a reference current tracking control does not need absolute and exact air gap signal. A gap signal with error offset and low noise variance is sufficient to achieve stable levitation. Since exact position depends on the total weight of the levitating object, we are of opinion that to give up exact position for gaining low cost device using sensorless method is an efficient bargain. Therefore, in this chapter we introduce this smart combination and experimentally verify the claim. This has the potential of being a robust and low cost solution for magnetically levitated carriers in industrial applications.

5.2 Permanent Magnet Assisted EML Model

In order to apply zero power control, the experimental test bench is modified by attaching NdFeB permanent magnets to each pole as shown in Fig. 5.1. Due to the non-availability of PMs matching pole area, we proceeded with improvisation of the available sizes in

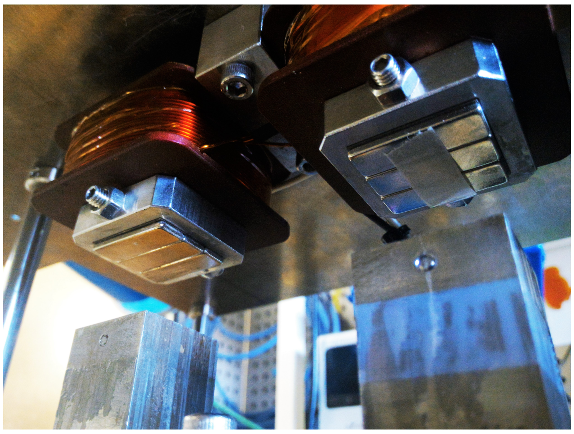

Figure 5.1: NdFeB magnets attached on each pole.

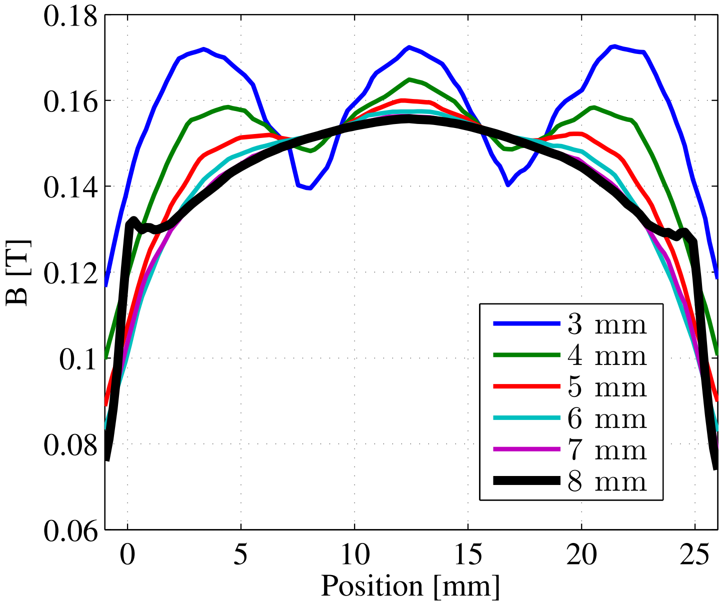

Figure 5.2: Magnetic field distribution due to three parallel placed permanent magnets.

the market. A set of three rectangular permanent magnets are attached parallel on each pole face. For large air gaps, this configuration has negligible effect on the magnetic field distribution, verified by numerical simulation as shown in Fig. 5.2. Next, permanent magnet assisted EML model is derived. The dynamic equations for electrical and mechanical domains are similar to the ones used in Chapter 2. The only change is in the magnetic circuit and its relevant equations. The modified free body diagram and its corresponding magnetic circuit is shown in Fig. 5.3. In Fig. 5.3(b), permanent magnet is modeled as source of magnetomotive force $H_c l_m$ with inherent reluctance $\mathcal{R}_m$ given as:

$$\mathcal{R}_m = \frac{l_m}{\mu_m A_m} \tag{5.1}$$

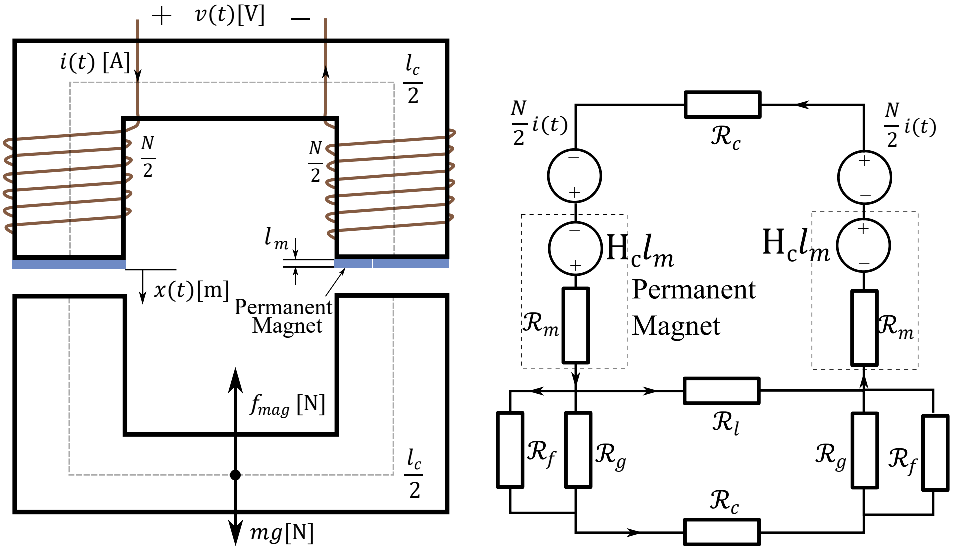

(a) (b)

Figure 5.3: (a) Electromagnetic Levitation (EML) Model. (b) Magnetic circuit with permanent magnets.

Where l_m is the thickness of magnet, A_m is its area which is equal to pole area in this case and μ_m is recoil permeability of PM which approximately equal to u_0. Solving the magnetic circuit:

$$\begin{aligned} Ni(t) + 2H_c l_m &= \phi(t)\big(2\mathcal{R}_c + 2\mathcal{R}_g + 2\mathcal{R}_m\big) \\ Ni(t) + 2H_c l_m &= B_g A\big(2\frac{l_c}{2\mu_r\mu_0 A} + 2\frac{x(t)}{\mu_0 A} + 2\frac{l_m}{\mu_0 A}\big) \\ B_g &= \frac{\mu_0\big(Ni(t) + 2H_c l_m\big)}{2x(t) + 2l_m + \frac{l_c}{\mu_r}} \end{aligned} \tag{5.2}$$

Where we have ignored leakage and fringing effects, and used same pole area for all three reluctances. Using principle of virtual displacement [28], total magnetic force f_{mag} is calculated as:

$$f_{mag} = \frac{\partial W_g}{\partial x} = \frac{\mu_0 A\Big(Ni(t) + 2H_c l_m\Big)^2}{\Big(2x(t) + 2l_m + \frac{l_c}{\mu_r}\Big)^2} \tag{5.3}$$

Where W_g is the energy stored within the gap given as:

$$W_g = \frac{1}{2}\frac{B_g^2}{\mu_0}2Ax(t)$$

By using definition of inductance, f_{mag} can be expressed as:

$$f_{mag} = -\frac{1}{2}\frac{\partial L(x)}{\partial x}(i(t) + i_m)^2 \tag{5.4}$$

Where the effect of PM has been represented as constant equivalent current $i_m = \frac{2H_c l_c}{N}$. This facilitates identification of plant parameters by reducing experimental requirements to just $L(x)$ profile and $i_m = \sqrt{\frac{2mg}{-\frac{\partial L}{\partial x}}}$. i_m is experimentally measured by keeping $i(t) = 0$ and varying the gap length from small to large values until the levitating object falls down. Air gap value at such instant is noted down from which $\frac{\partial L}{\partial x}$ is calculated. Remaining required parameter is mg only. Thus i_m's experimental value is known.

In order to design zero power control, the dynamic equations (2.1) and (2.2) are linearized at operating point $(x_0, v_0, i_0) = (x_0, 0, 0)$. Assuming $x(t) = x_0 + \Delta x(t)$, $i(t) = i_0 + \Delta i(t)$, $v(t) = v_0 + \Delta v(t)$, linearized plant is given as:

$$\begin{bmatrix}\Delta\dot{x}(t)\\ \Delta\ddot{x}(t)\\ \Delta\dot{i}(t)\end{bmatrix} = \begin{bmatrix}0 & 1 & 0\\ -\frac{k_x}{m} & 0 & -\frac{k_i}{m}\\ 0 & \frac{k_i}{L_0} & -\frac{R}{L_0}\end{bmatrix}\begin{bmatrix}\Delta x(t)\\ \Delta\dot{x}(t)\\ \Delta i(t)\end{bmatrix} + \begin{bmatrix}0\\ 0\\ \frac{1}{L_0}\end{bmatrix}\Delta v(t) \tag{5.5}$$

Where

$$k_x = -\frac{1}{2}\frac{\partial^2 L}{\partial x^2}(i_m)^2 \quad k_i = -\frac{\partial L}{\partial x}(i_m) \quad L_0 = \frac{\mu_0 A N^2}{2x_0 + 2l_m + \frac{l_c}{\mu_r}} \quad f_{mag}\Big|_{(x_0,v_0,i_0)} = mg$$

5.3 Sensorless EML with zero power control

The proposed combination is shown in Fig. 5.4. The only input to the digital computer using sensor is coil current. Furthermore, due to zero power control the power consumption is minimal. Hence this combination produces a cost effect EML system with low initial and operating cost. In the design of the controller, air gap detector is taken as a noisy sensor and conventional method of designing state feedback controller is used. Pole placement is done by using the Manabe's canonical form to ensure stable closed loop system.

For zero power control the input to the plant is:

$$\Delta v(t) = -\mathbf{K}\mathbf{x} + k_e x_e \tag{5.6}$$

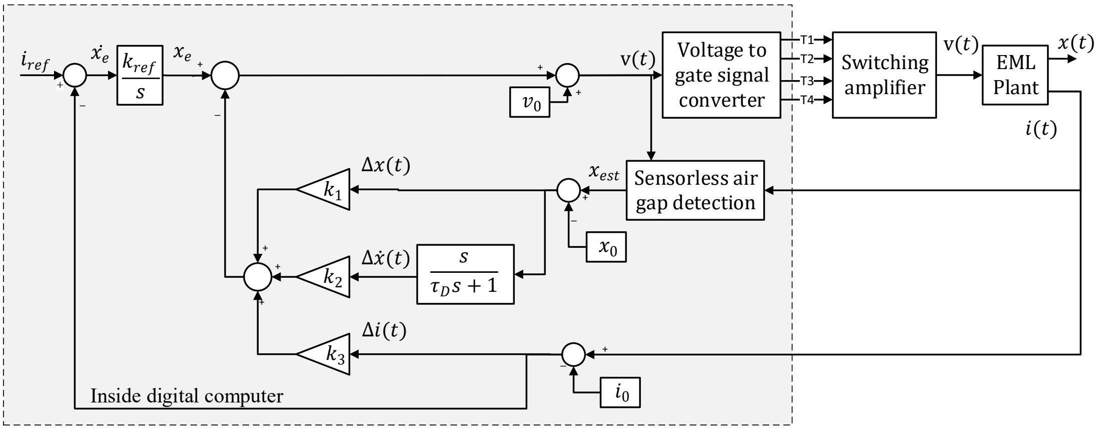

Figure 5.4: Sensorless EML with zero power control.

Where $\dot{x_e} = i_{ref} - \Delta i(t)$, $\mathbf{K} = [k_1, k_2, k_3]$ and k_e is the integral gain. The closed loop system is derived as :

$$\begin{bmatrix} \dot{\mathbf{x}} \\ \dot{x_e} \end{bmatrix} = \underbrace{\begin{bmatrix} 0 & 1 & 0 & 0 \\ -\dfrac{k_x}{m} & 0 & -\dfrac{k_i}{m} & 0 \\ -\dfrac{k_1}{L_0} & \dfrac{k_i}{L_0} - \dfrac{k_2}{L_0} & -\dfrac{R}{L_0} - \dfrac{k_3}{L_0} & \dfrac{k_e}{L_0} \\ 0 & 0 & -1 & 0 \end{bmatrix}}_{\mathbf{A}'} \begin{bmatrix} \mathbf{x} \\ x_e \end{bmatrix} + \begin{bmatrix} 0 \\ 0 \\ 0 \\ 1 \end{bmatrix} i_{ref} \tag{5.7}$$

Solving $s\mathbf{I} - \mathbf{A}' = 0$, the characteristic polynomial obtained is:

$$\begin{aligned} s^4 + \left(\frac{R}{L_0} + \frac{k_3}{L_0}\right)s^3 + \left(\frac{k_i^2}{mL_0} - \frac{k_i k_2}{mL_0} + \frac{k_x}{m} + \frac{k_e}{L_0}\right)s^2 \\ + \left(\frac{k_x R}{mL_0} + \frac{k_x k_3}{mL_0} - \frac{k_i k_1}{mL_0}\right)s + \frac{k_e k_x}{mL_0} = 0 \end{aligned} \tag{5.8}$$

Using Manabe's method [27], for a 4th order polynomial

$$s^4 + \frac{(2.5)(2)(2)}{\tau_z}s^3 + \frac{(2.5^2)(2^2)(2)}{\tau_z^2}s^2 + \frac{(2.5^3)(2^2)(2)}{\tau_z^3}s + \frac{(2.5^3)(2^2)(2)}{\tau_z^4} = 0 \tag{5.9}$$

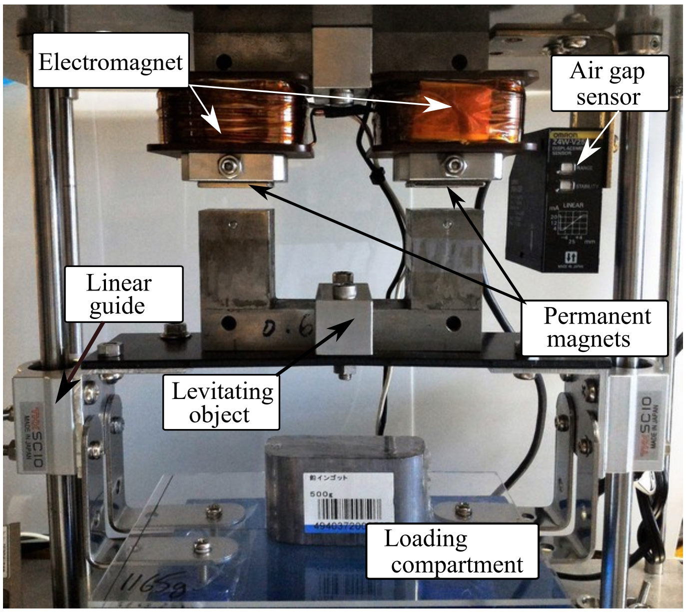

Figure 5.5: Experimental test bench with permanent magnets.

Where τ_z is the time constant for tuning controller's speed. The gain matrix $\mathbf{K}$ and k_e are calculated using (5.8) and (5.9) as:

$$
\begin{aligned}
k_1 &= \left(k_x R + k_x k_3 - \frac{(2.5^3)(2^2)(2)}{\tau_z^3} m L_0\right)\frac{1}{k_i} \\
k_2 &= \left(\frac{k_i^2}{m L_0} + \frac{k_x}{m} + \frac{k_e}{L_0} - \frac{(2.5^2)(2^2)(2)}{\tau_z^2}\right)\frac{m L_0}{k_i} \\
k_3 &= \frac{(2.5)(2)(2)}{\tau_z} L_0 - R \\
k_e &= \frac{(2.5^3)(2^2)(2) m L_0}{\tau_z^4 k_x}
\end{aligned}
$$

Table 5.1: Parameter Values used in Experiments

Parameters	**Value**	**Parameters**	**Value**
m [kg]	1.165	T_s[sec]	1.25×10^{-6}
V_{dc} [V]	45	T_{pwm} [sec]	2×10^{-3}
R [Ω]	1.7	x_0 [m]	5.5×10^{-3}
i_0 [A]	0	i_m[A]	4.24
l_m[m]	2×10^{-3}	L_0 [H]	25.2×10^{-3}
k_i [N/A]	5.35	k_x [N/m]	-2.85×10^3
τ_z [sec]	0.075	k_1 [A/m]	-3407
k_2[As/m]	-65.5	k_3 [V/A]	1.65
k_e[V/As]	-5	δD	0.4

5.4 Experimental Verification

The benefits of this smart combination are experimentally verified on a test bench shown in Fig. 5.5. The parameters of experimental test bench and controller are given in Table 5.1.

The experimental results for the proposed smart pair are presented in Fig. 5.6. At first, an additional weight of 0.88[kg] is added (Fig. 5.6(a)) and removed (Fig. 5.6(b)) to demonstrate the change of position for a zero average coil current. Results show that there remains a constant offset error between $x(t)$ and x_{est}, attributed to the modeling error of inductance profile which is almost impossible to remove due to the low sensitivity nature of inductance at the large air gap. But since the objective of zero power control is to maintain zero average current i.e reference current tracking, exact and absolute air gap signal seems redundant. **It is emphasized here, that a signal having an error offset with low noise variance such as x_{est} is sufficient to maintain stable levitation. Since exact position depends on the total weight of the levitating object, the author feels that it is an efficient bargain to give up exact position for gaining low cost device using sensorless method**. Furthermore, Fig. 5.6(c) and Fig. 5.6(d) show that for most part, $\alpha{\approx}0.5$ which ensures minimal noise variance for our air gap detection method.

However, addition of PM into magnetic path results in increase of total magnetic path reluctance. PM consumes the available physical gap length between fixed core and mover. For instance, previously for just EML system the mechanical gap length was 8[mm], but since $l_m = 2$[mm], now the available gap length reduces to 6[mm]. This shifts the $L(x)$ vs $x(t)$ profile towards left as shown in Fig. 5.7. Since sensorless method's output noise strongly depends on sensitivity of inductance to air gap $\frac{\partial L}{\partial x}$, the decrease in $\frac{\partial L}{\partial x}\Big|_B$ for the operating point x_0 in zero power control produces high variance noise, compared to the case ($\frac{\partial L}{\partial x}\Big|_A$) when there is no PM.

Stable levitation time profile for two cases ($x_0 = 5.5$[mm], $x_0 = 8$[mm]) is shown in Fig. 5.8. The levitation profile for $x_0 = 8$[mm] is oscillatory owing to the aforementioned reasons. Furthermore, loading and unloading results for $x_0 = 8$[mm] are also shown in Fig. 5.9. In Fig. 5.9(a) it can be seen that at time of loading, the air gap increases beyond air gap sensor's range which is shown as a horizontal line. But since sensorless method has no such limitation, it allows successful levitation. To obtain $i(t) = 0$ at large air gap requires a new design of PM and modification to the test bench accordingly. Therefore, for testing purpose only, $x_0 = 8$[mm] is achieved by setting $i_{ref} = 2$[A]. This step emulates a stronger PM with increased i_m=$(4.24 + 2)$[A].

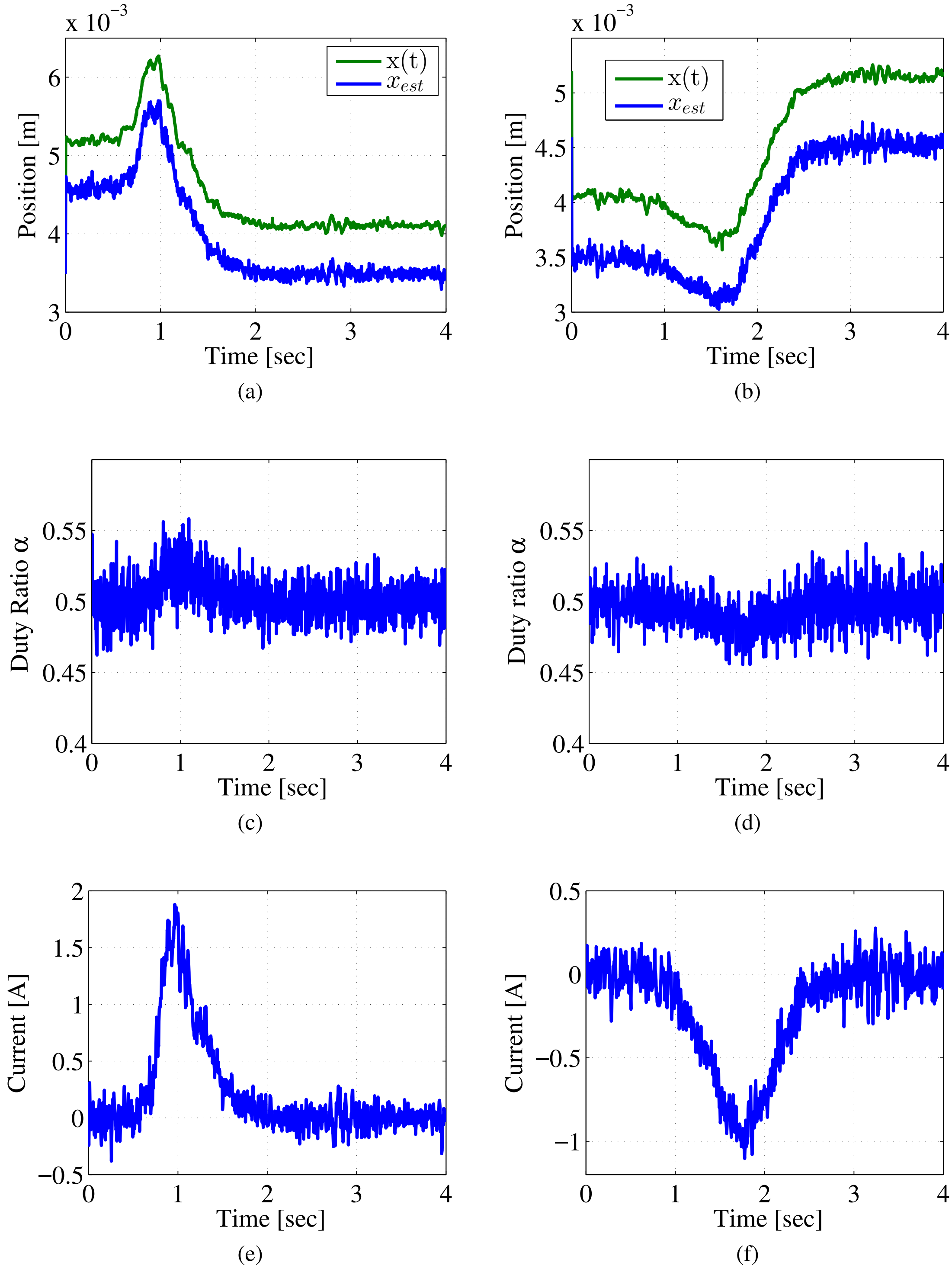

Figure 5.6: Weight loading: (a) Position. (c) Duty ratio α. (e) Average coil current. Weight unloading: (b) Position. (d) Duty ratio α. (f) Average coil current.

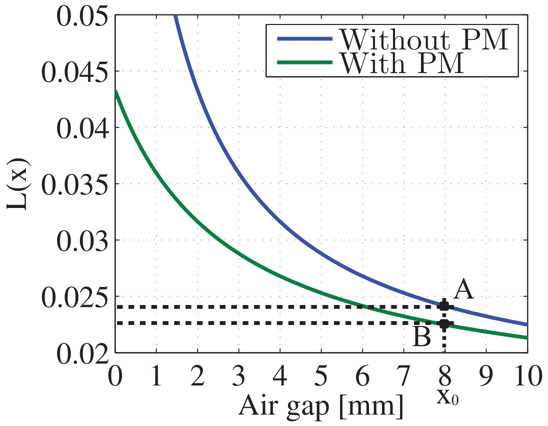

Figure 5.7: Inductance shift due to insertion of PM in magnetic path resulting in decrease in sensitivity to air gap.

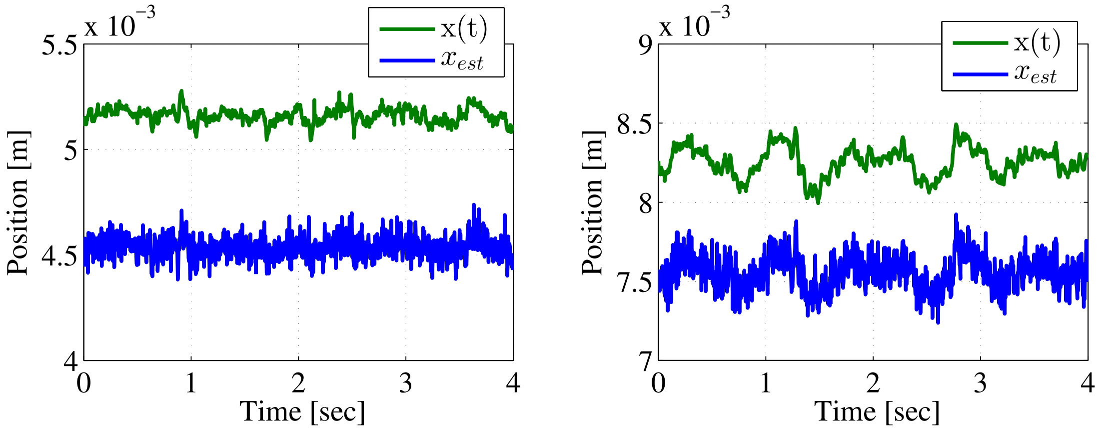

(a)

(b)

Figure 5.8: Stable levitation profile: (a) At $i_{ref} = 0$[A] , $x(t) \approx 5.5$[mm]. (b) At $i_{ref} = 2$[A] , $x(t) \approx 8$[mm].

5.4.1 Possible Improvements for sensorless EML with zero power control

To achieve low noise variance at large air gap as was the case without PM, magnetic path should be optimized. One possible way to achieve it is shown in Fig. 5.10. This kind of topology was proposed by [31]. A thin slice of permanent magnet is buried inside the core. Moreover, instead of a constant core area, area of PM is maximized and length is minimized to achieve same bias flux for supporting load. This way PM consumes less mechanical air gap. Consequently, decrease in $\frac{\partial L}{\partial x}$ is reduced, allowing oscillation free levitation at large gap lengths.

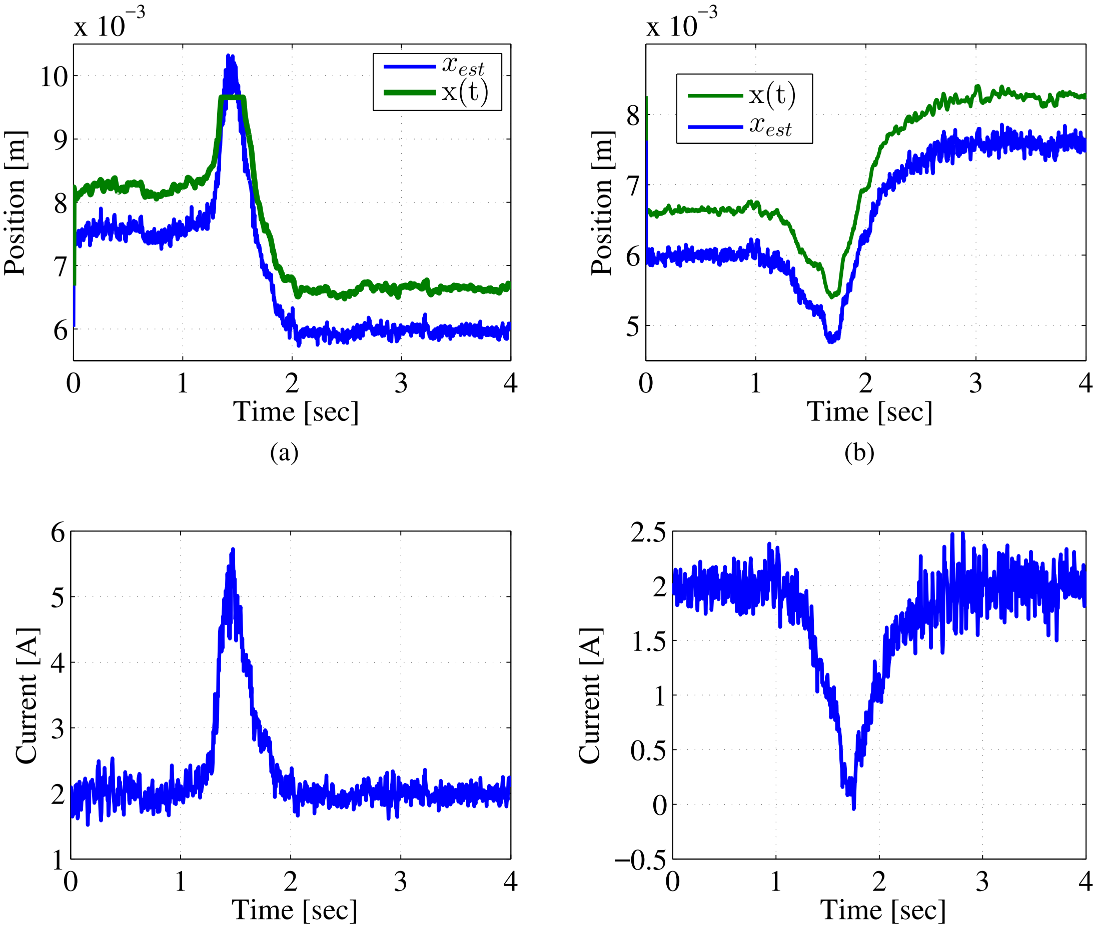

(a) (b)

(c) (d)

Figure 5.9: Weight loading: (a) Position. (c) Average coil current. Weight unloading: (b) Position. (d) Average coil current.

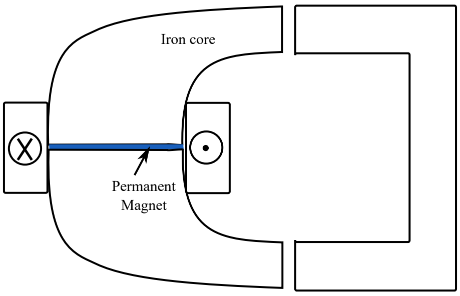

Figure 5.10: Improved core design with PM to minimize decrease in sensitivity $\frac{\partial L}{\partial x}$

Chapter 6

Conclusion

In conclusion, this research has demonstrated two novel ideas. The first one is the improvement in the sensorless methods as well as their implementations for large air gap translation motion application. Sequentially, novel methods for air gap detection have been proposed and verified experimentally. Single slope detection method, which has good robustness to duty ratio variation has been demonstrated first. Identification of its shortcomings has resulted to resistance estimation algorithm. Following that, weighted current-ripple slope measurement method which is an amalgam of double slopes and single slope methods has been proposed. It has been statistically shown to posses low noise variance as well as good robustness to variation of duty ratio. Rational steps have been taken to decide the parameters for weights. Apart from the method itself, a noise suppression strategy has been proposed. The strategy is a combination of the conventional concepts of state observer and disturbance observer to suppress the propagated noise from current sensor to the air gap. Tuning parameters of state observer have been reduced down to just one. This allows ease of use for engineer in practical environment.

The second novelty is more of an opinion related, which includes a smart combination of our sensorless method with zero power control. We have claimed and experimentally proved that zero power control is the best control law to be combined with sensorless EML since each enhances other's performances. Since zero power control is a reference current tracking control, absolute air gap information which is usually obtained by expensive displacement sensors has been shown to be redundant and is a viable trade off for a low noise variance signal obtain via sensorless method with possible error offset. Furthermore, it has been shown that for zero power control duty ratio remains around 0.5 which is the optimal case for sensorless EML. This also minimized operational cost for EML system producing a cost effective EML solution for industrial conveyor systems. These ideas have contributed in advancing the EML technology to provide simple, robust and low cost applications for industry use.

6.1 Future Works

The present work has been demonstrated for a single degree of freedom EML system. Whereas in practical application, complex topologies for EML are used. Therefore, in future suitable higher degree of motion EML topologies shall be designed with ease of sensorless method's application in mind. For magnetically levitated conveyor systems, a thrust mechanism is also required which is usually provided by a linear machine. Integrating EML plant with linear machine can have unfavorable effects on sensorless detection. Therefore, analysis of such integration shall also be studied. Some explicit steps for future are given below:

- Expand research scope to complex electromagnetic topologies.
- Increase ease of application.(Using ONLY numerical modeling, without obtaining experimental database beforehand). From the view point of industrial manufacturing and testing, this can be an efficient method to save production cost.
- Improve hardware specifications.
  - Sensorless method using current-ripple slope measurement requires strict noise limitations on sensed current signal. By using good quality current sensors and data acquisition hardware, it is possible to allow for shorter T_{pwm}, consequently a better dynamic response can be achieved.
- Proposal of a new EML structure which can provide higher degree of motion freedom. In order to remove linear guides, the proposed structure must have adequate stiffness in suspension and guidance.
- Sensorless method can also be used to obtain signals for guidance clearance.
- Design of a linear actuator.
  - Optimization of the designed linear actuator structure for sensorless EML.
- Integrate EML with linear actuator.
  - Design of decoupled control.
  - Maintaining a simple, robust and low cost structure.
- Additional prospective steps.
  - Looking for further cost reduction by linear encoder-less drive.
    - A crude idea: Use of the already existing sensorless levitation to detect linear motion.

List of Publications

1. S. Ahmed and T. Koseki, "Air-Gap Sensorless State Estimation for Electromagnetic Levitation Control Using Measured Ripple Current Slope" Technical meeting on Linear Drives, IEE Japan, LD-16-006, Jan. 2016,
2. S. Ahmed, V. D. Duc, and T. Koseki. “Electromagnetic levitation control with sensorless large air gap detection for translational motion application using measured current-ripple slope”. In: *Industrial Electronics Society, IECON 2016 - 42st Annual Conference of the IEEE*. 2016 (To be presented)
3. S. Ahmed and T. Koseki. “Noise suppression strategy for sensorless electromagnetic levitation using current-ripple measurement method with extended operational range of duty ratio”. In: *Electrical Machines and Systems (ICEMS), 2016 19th International Conference on*. 2016 (To be presented)
4. S. Ahmed and T. Koseki. “Smart combination of sensorless electromagnetic levitation and zero power control: A complimentary pair enhancing mutual strengths”. In: *Mechatronics (ICM), 2017 IEEE International Conference on*. 2017 (Submitted for review)

Bibliography

[1] M. E. Hoque et al. “Development of a three-axis active vibration isolator using zero-power control”. In: *IEEE/ASME Transactions on Mechatronics* 11.4 (2006), pp. 462–470. ISSN: 1083-4435. DOI: 10.1109/TMECH.2006.878536.

[2] URL: http://www.transrapid.de/pics/.

[3] URL: http://linear-museum.pref.yamanashi.jp/gallery/photo/index.html/.

[4] URL: http://www.magneticbearings.org/.

[5] Y. M. Choi and D. G. Gweon. “A High-Precision Dual-Servo Stage Using Halbach Linear Active Magnetic Bearings”. In: *IEEE/ASME Transactions on Mechatronics* 16.5 (2011), pp. 925–931. ISSN: 1083-4435. DOI: 10.1109/TMECH.2010.2056694.

[6] Jiangheng Liu and T. Koseki. “3 degrees of freedom control of semi-zero-power magnetic levitation suitable for two-dimensional linear motor”. In: *Electrical Machines and Systems, 2001. ICEMS 2001. Proceedings of the Fifth International Conference on*. Vol. 2. 2001, 976–981 vol.2. DOI: 10.1109/ICEMS.2001.971842.

[7] H. Hayashiya, H. Ohsaki, and E. Masada. “A combined lift and propulsion system of a steel plate by transverse flux linear induction motors”. In: *IEEE Transactions on Magnetics* 35.5 (1999), pp. 4019–4021. ISSN: 0018-9464. DOI: 10.1109/20.800741.

[8] C. H. Kim et al. “Levitation and thrust control of a Maglev LCD glass conveyor”. In: *IECON 2011 - 37th Annual Conference on IEEE Industrial Electronics Society*. 2011, pp. 610–615. DOI: 10.1109/IECON.2011.6119380.

[9] M. Morishita et al. “A new MAGLEV system for magnetically levitated carrier system”. In: *IEEE Transactions on Vehicular Technology* 38.4 (1989), pp. 230–236. ISSN: 0018-9545. DOI: 10.1109/25.45486.

[10] Takeshi Mizuno and Yuichiro Takemori. “A transfer-function approach to the analysis and design of zero-power controllers for magnetic suspension systems”. In: *Electrical Engineering in Japan* 141.2 (2002), pp. 67–75. ISSN: 1520-6416. DOI:

10.1002/eej.10049. URL: http://dx.doi.org/10.1002/eej.10049.

[11] Maslen Eric H. (Eds.) Schweitzer Gerhard. *Magnetic Bearings. Theory, Design, and Application to Rotating Machinery*. 2009.

[12] D. Vischer and H. Bleuler. “Self-sensing active magnetic levitation”. In: *Magnetics, IEEE Transactions on* 29.2 (1993), pp. 1276–1281. ISSN: 0018-9464. DOI: 10.1109/20.250632.

[13] N. Morse et al. “Position sensed and self-sensing magnetic bearing configurations and associated robustness limitations”. In: *Decision and Control, 1998. Proceedings of the 37th IEEE Conference on*. Vol. 3. 1998, 2599–2604 vol.3. DOI: 10.1109/CDC.1998.757843.

[14] K. Okada Y. Matsuda and B. Nagai. “Sensorless Magnetic Levitation Control by Measuring the PWM Carrier Frequency Component”. In: *International Symbosium on Magnetic Bearings*. 1992.

[15] Eric H. Maslen, Dominick T. Montie, and Tetsuya iwasaki. “Robustness Limitations in Self-Sensing Magnetic bearings”. In: *Journal of Dynamic Systems, Measurement, and Control* (2006).

[16] A. Schammass et al. “New results for self-sensing active magnetic bearings using modulation approach”. In: *Control Systems Technology, IEEE Transactions on* 13.4 (2005), pp. 509–516. ISSN: 1063-6536. DOI: 10.1109/TCST.2004.843142.

[17] M.D. Noh and Eric H. Maslen. “Self-sensing magnetic bearings using parameter estimation”. In: *Instrumentation and Measurement, IEEE Transactions on* 46.1 (1997), pp. 45–50. ISSN: 0018-9456. DOI: 10.1109/19.552155.

[18] E.O. Ranft, G. van Schoor, and C.P. du Rand. “Self-sensing for electromagnetic actuators. Part II: Position estimation”. In: *Sensors and Actuators A: Physical* 172.2 (2011), pp. 410 –419. ISSN: 0924-4247. DOI: http://dx.doi.org/10.1016/j.sna.2011.09.037.

[19] Lichuan Li, T. Shinshi, and A. Shimokohbe. “State feedback control for active magnetic bearings based on current change rate alone”. In: *Magnetics, IEEE Transactions on* 40.6 (2004), pp. 3512–3517. ISSN: 0018-9464. DOI: 10.1109/TMAG.2004.836295.

[20] Andries C. Niemann, George van Schoor, and Carel P. du Rand. “A Self-Sensing Active Magnetic Bearing Based on a Direct Current Measurement Approach”. In: *Sensors* 13.9 (2013), p. 12149. ISSN: 1424-8220. DOI: 10.3390/s130912149.

[21] Jinou Wang and A. Binder. "Self-sensing magnetic bearings using multiple sampling of currents alone". In: *Power Electronics and Applications (EPE), 2013 15th European Conference on*. 2013, pp. 1–10. DOI: 10.1109/EPE.2013.6631872.

[22] Jinou Wang and A. Binder. "Current slope calculation in FPGA for sensorless control technique and associated slope based predictive precise current control". In: *Sensorless Control for Electrical Drives and Predictive Control of Electrical Drives and Power Electronics (SLED/PRECEDE), 2013 IEEE International Symposium on*. 2013, pp. 1–8. DOI: 10.1109/SLED-PRECEDE.2013.6684508.

[23] J. Wang and Binder. "Position Estimation for Self-Sensing Magnetic Bearings Based on Double Detection of Current Slopes". In: *14th International symposium on Magnetic Bearings* (2014).

[24] A.H. Ranjbar, R. Noboa, and B. Fahimi. "Estimation of Airgap Length in Magnetically Levitated Systems". In: *Industry Applications, IEEE Transactions on* 48.6 (2012), pp. 2173–2181. ISSN: 0093-9994. URL: 10.1109/TIA.2012.2226855.

[25] T. Gluck et al. "A novel robust position estimator for self-sensing magnetic levitation systems based on least squares identification". In: *Control Engineering Practice* 19.2 (2011), pp. 146 –157. ISSN: 0967-0661. DOI: http://dx.doi.org/10.1016/j.conengprac.2010.11.003.

[26] Michael Richter, Hendrik Schaede, and Stephan Rinderknecht. "Investigations on the "Direct Digital Inductance Estimation" - Concept for Self-Sensing AMBs Under Influence of Eddy Currents". In: *International Symposium on Magnetic Bearings*. 2014.

[27] S. Manabe. "The coefficient diagram method". In: *14th IFAC Symposium on Automatic Control in Aerospace*. 1998.

[28] A. E. Fitzgerald. *Electric Machinery. A.E. Fitzgerald, Charles Kingsley, JR., Stephen D. Umans*. 6th. McGraw-Hill. ISBN: 0071230106.

[29] P.K. Sinha. *Electromagnetic Suspension: Dynamics & Control*. IEE control engineering series. P. Peregrinus, 1987. ISBN: 9780863410635. URL: https://books.google.co.jp/books?id=DRdtKenSW1UC.

[30] A. Radke and Zhiqiang Gao. "A survey of state and disturbance observers for practitioners". In: *2006 American Control Conference*. 2006, 6 pp.–. DOI: 10.1109/ACC.2006.1657545.

[31] Hellmut Horn. "Stabile magnetische Fahrzeugstützung mit permanentmagnetischer Erregung". Zugl.: Braunschweig, Techn. Univ., Diss., 1994.

[32] S. Ahmed, V. D. Duc, and T. Koseki. “Electromagnetic levitation control with sensorless large air gap detection for translational motion application using measured current-ripple slope”. In: *Industrial Electronics Society, IECON 2016 - 42st Annual Conference of the IEEE*. 2016 (To be presented).

[33] S. Ahmed and T. Koseki. “Noise suppression strategy for sensorless electromagnetic levitation using current-ripple measurement method with extended operational range of duty ratio”. In: *Electrical Machines and Systems (ICEMS), 2016 19th International Conference on*. 2016 (To be presented).

[34] S. Ahmed and T. Koseki. “Smart combination of sensorless electromagnetic levitation and zero power control: A complimentary pair enhancing mutual strengths”. In: *Mechatronics (ICM), 2017 IEEE International Conference on*. 2017 (Submitted for review).